

UNIVERSITÀ DEGLI STUDI ROMA TRE

Dipartimento di Ingegneria Elettronica
Dottorato di Ricerca
Ingegneria Elettronica: dalle Nanostrutture ai Sistemi
XXI Ciclo

Fotonica Nonlineare a Picosecondi

Tesi di Dottorato di ricerca in Ingegneria Elettronica

Alessia Pasquazi

Relatore
Prof. Gaetano Assanto

Coordinatore del Corso di Dottorato
Prof. Gennaro Conte

2009

NONLINEAR PHOTONICS WITH PICOSECONDS

Alessia Pasquazi

A dissertation submitted to the University of Rome “Roma Tre”
for the degree of Doctor of Philosophy in Electronic Engineering

2009

Acknowledgements

I am indebted to several people who helped and supported me during my PhD. The Nonlinear Optics and Optoelectronics Lab has been a stimulating environment, providing me with good friends and scientific expertise.

Prof. Gaetano Assanto supervised this work, and I am grateful to him for his competence and for providing motivations and opportunities to develop my scientific curiosity. From him I have learned how to do research even during hard times. Dr. Salvatore Stivala shared with me the whole time I spent at the 10Hz source and collected all the experimental data on the SPP-LN samples. I found in him a patient, critical and reliable colleague when facing difficulties and the unpredictable challenges set out by the laser. Salvatore remains, most of all, a true friend. I express all my gratitude to Dr. Lorenzo Colace, on whose door I often knocked when looking for help when the source ran out of control. He always helped, no matter how busy he was. I learned a lot from his expertise in the field.

I thank all the collaborators who made possible this work by providing samples, competence and new ideas: Dr. Alessandro Busacca for the ferroelectric waveguides, Dr. Jose' Gonzalo for the heavy metal oxide glasses, Prof. Davide Comoretto for the colloidal opal and Dr. Katia Gallo for the hexagonally poled lithium niobate. She was also with me at the optical bench during the picoseconds measurements on the HexLN sample. I thank Prof. Decio Levi, who introduced me to the analysis of nonlinear differential equations and patiently answered the many questions of an electronic engineer struggling with advanced math.

I have to mention all the guys in the lab, my “scientific family”: I could always (and still can) count on them: in rigorous alphabetical order Alessandro Alberucci, Michele Balbi, Jisha Chandrot Pannian, Andrea Di Falco, Andrea Fratalocchi, Armando Piccardi, Usman Sapaev and Vito Sorianello. My best wishes to the newcomers Elena and Schirin to be as lucky as I was in finding my scientific way and so many friends. I thank my family who loved, supported, fed me and listened to me. In particular I am grateful Guido, for having soldered what I could not.

but certainly not least I thank my husband Marco Peccianti, who helped me to focus on and overcome my problems, with competent advices and thorough understanding.

Contents

1	In situ tuning of a colloidal opal with picosecond pulses	9
1.1	Au-np doped polystyrene opal	10
1.2	Experiments and data reduction	11
1.3	Conclusion	15
2	Transverse Nonlinear Optics in Heavy Metal Oxide Glasses	16
2.1	Self-confined beam and catastrophic collapse	17
2.2	Material Properties and Experimental Setup	17
2.2.1	Self-focusing and Spatial Solitons	18
2.2.2	Modulation Instability and Multiple Filamentation	22
2.3	Conclusions	25
3	Guided-wave Second Harmonic Generation in Surface Periodically Poled Ferroelectrics	26
3.1	Surface periodically poled for frequency doubling	26
3.2	Frequency doubling in SPP LN waveguides @1550nm	27
3.3	Ultra-Violet Generation in Periodically-Poled Lithium Tantalate Waveguides	33
3.4	Conclusions	35
4	Spatial Simultons in Quadratic Nonlinear Lattice	36
4.1	Derivation of the Governing Equations	37
4.1.1	No depletion plane-wave regime	38
4.1.2	General case	41
4.2	Analysis of the governing Equations	42
4.2.1	Symmetric case	44
4.2.2	Asymmetric case	51
4.3	Experiments on simultons in a 2D nonlinear lattice: HexLN	54
4.3.1	HexLN planar waveguide and experimental setup	54
4.3.2	Observation of Quadratic Spatial Solitons in a HexLN waveguide	55
4.4	Conclusions	63
5	Conclusions	64
	Bibliography	65

Preface

Utere temporibus (Ovid)

To introduce the work reported in this thesis I start with three key words: *Photonics*, *Nonlinear* and *Time*. Optics and photonics are two closely connected words. “Opticks” was used by Newton in his treatise on light and -historically- is the word which defines the science of light. “Photonics” is a term of our times, which reflects the mixing of technology and science of modern age; initially introduced with the meaning “electronics of photons”, it now possesses a broader significance for someone embracing optics itself. The root of this word is found in the introduction to the concept of photon by Einstein, in the first years of the last century; however, only the discovery of lasers in the sixties[1] made possible the conversion of optics into photonics. The birth of this “new and old” science triggered a revolution in several fields, like telecommunications, material science and biology, with new developments dramatically linked to the understanding and the control of phenomena in novel materials and structures. In this scenario a key role is played by nonlinearity.

The adjective Nonlinear can be misleading, as it has a negative connotation, implying the lack of something. On the contrary, it has to be regarded as positive, because the nonlinear world possesses a larger number of degrees of freedom compared to the linear one. In a certain sense nonlinearity helps photonics to be “more electronic”: when effects can be mixed instead of “superimposed” as in the linear case, light can be controlled by light itself. In addition, nonlinearity helps photonics to be “more interdisciplinary”, some nonlinear phenomena being ubiquitous and shared by diverse physical systems.

Outstanding examples of universal phenomena are solitary waves, noticed for the first time by Scott Russell in a shallow water channel near Edinburgh and later studied in plasma physics, Bose-Einstein condensates, neuroscience and, of course, optics. Optical bright spatial solitons are self-guided beams propagating without diffraction via self-focusing[2]; they have been attracting attention since the early 60’s and represent one of the most fascinating topics in nonlinear optics: the possibility of guiding and processing light make spatial solitons promising for future applications in all optical networks and has motivated great efforts towards designing and demonstrating soliton based devices in several materials.

Wave dynamics in periodic structures represents another widespread topic, peculiar of electrons in crystals and discovered in light about a decade ago in Photonic Crystals[3]. The latter are structures encompassing a modulation of the dielectric constant with period of the order of the wavelength; as their electronic counterparts they can exhibit

a band-gap, forbidding light propagation in certain directions at specific wavelengths. Photonic Crystal-based structures can therefore enhance confinement, guidance, filtering, switching and -generally- processing of light through its interactions with matter.

More interesting phenomena occur when nonlinear effects are connected with periodicity. A field of primary importance in nonlinear optics is frequency conversion, mainly investigated by using quadratic materials. The first experiment was carried out in 1961 (Franken *et al.*)[4], when the light of a ruby laser was converted to ultraviolet using a quartz crystal; this effect is employed nowadays to generate a wide range of frequencies otherwise impossible to obtain with conventional lasers. A popular technique to efficiently convert light consists in creating a periodic quadratic coefficient in the material: the induced grating helps momentum conservation in the photon conversion process, playing an essential role in the efficiency. New geometries for light conversion can be designed when the modulation of the quadratic coefficient takes place in more than one dimension.

Nonlinear effects as those described above can be observed only using strong excitations that must be properly dosed to unveil the sought phenomena. The pulse duration of the light source can play a crucial role in the correct management between bandwidth and energy, allowing the excitation of the desired effect. The work in this thesis is mainly experimental, accompanied by theoretical-numerical analyses when needed. A highly energetic picoseconds tunable source is the most appropriate tool for exciting the effects reported here and touching upon a few areas of growing interest in nonlinear photonics. These effects are discussed, whenever possible, following a “logical flux” instead of a chronological one, making the report more easily readable.

Chapter 1 addresses an experiment for in situ tuning of a Colloidal Opal; a brief introduction to (linear) periodic structures and photonic crystals (PC) is provided. Opals are the simplest and most accessible three dimensional photonic crystals, although their band gap is often incomplete; their template consists of closely packed spheres which can be infiltrated and used as a playground to test materials and concepts. In a photonic scenario where several PC-elements are integrated to perform various signal-processing functions, fine adjustment and control of the individual band-gaps and their resonance is essential to the operation of these novel generations of optoelectronic chips. The sample used in the experiments is a polystyrene opal doped with gold nanoparticles (Au-np), with band gap in the C-band for telecommunications. By exploiting the Au-np plasmonic resonance in the visible, fine and controllable band gap tuning in selected areas of the composite opal is experimentally demonstrated, with resulting resonance shifts as large as 30 nm in the near-infrared - following sample illumination with picosecond pulses at 532nm. The effect, somehow different from previous results on transient perturbations, consists of a permanent blue shift of the resonance, the latter being associated to a decrease of the refractive index. As the photonic crystal retains its lattice structure after laser tuning, the opal can be effectively integrated in more complex photonic chips, as its gap can be finely photo-adjusted in selected areas with picosecond pulses, even after realization and/or during test procedures.

Chapter 2 reports solitary propagation in a novel glass with an ultrafast and large nonlinear response; an introduction to third order nonlinear materials and spatial solitary propagation is given. The glass under study belongs to the family of Heavy Metal Oxides (HMO), a promising class for ultrafast photonics thanks to its extended transmittance and large linear (> 2) and Kerr nonlinear refractive indices with ultrafast response times. When sustained by an intensity-dependent response, spatial solitons in bulk tend to undergo catastrophic collapse unless additional effects intervene to arrest it. This is the reason why, despite the conspicuous number of soliton-based applications for all-optical signal processing, bulk solitary propagation in glass has been reported in a few cases only, due to the unstable nature of two-dimensional solitary propagation in Kerr materials. With this in mind, I studied theoretically and experimentally the propagation of single and multiple spatial solitons on the glass, clarifying the stabilizing role of nonlinear absorption in preventing catastrophic collapse. This first observation of picosecond 2D+1 self-confined wave propagation in bulk solids opens up opportunities for ultrafast soliton based signal processing in bulk glasses.

In Chapter 3 I report the investigation on quadratic processes in surface periodically poled ferroelectrics. Surface periodic poling for quasi-phase matching in ferroelectrics such as $LiNbO_3$ and $LiTaO_3$ was introduced as a technique to better control mark-to-space ratios, due to the recent quest for short domain lengths for harmonic generation of shorter wavelengths (as well as at counter-propagating wave mixing). This technology is expected to push forward some of the frontiers in backward harmonic generation by short period quasi phase matching, presently limited to high order interactions. I contributed to the characterization of the first samples realized with this novel technique in conjunction with proton exchanged waveguides in $LiNbO_3$ for frequency doubling from 1550nm and in $LiTaO_3$ for UV generation; in the former case I help interpreting the experimental results with a simple theoretical model, providing a useful tool for characterizing and optimizing surface periodic poling and quasi-phase matching.

The last chapter is devoted to spatial solitary propagation sustained by a quadratic nonlinearity in two-dimensional periodically poled crystals. The quadratic nonlinearity can be responsible for self-confined propagation of multifrequency (e. g. fundamental and second harmonic) spatial solitons or similtions. The recent advent of quadratic bidimensional periodically-poled structures, i.e. bidimensional lattices in the second-order susceptibility, has introduced novel and more versatile geometries for parametric interactions. I worked on the first experimental observation of spatial solitons in nonlinear 2D photonic lattices. The hexagonally poled $LiNbO_3$ sample, optimized for twin-beam Second Harmonic Generation at 1550 nm, presented several new features unique to this 2D QPM configuration. A theoretical and numerical study and some considerations on the stability of the solitary solution of the novel system of equations are also detailed.

Experimental setup

The source used in the experiments consists of an optical parametric amplifier/oscillator (OPA/OPO) pumped by both an amplified frequency-doubled pulse train and single

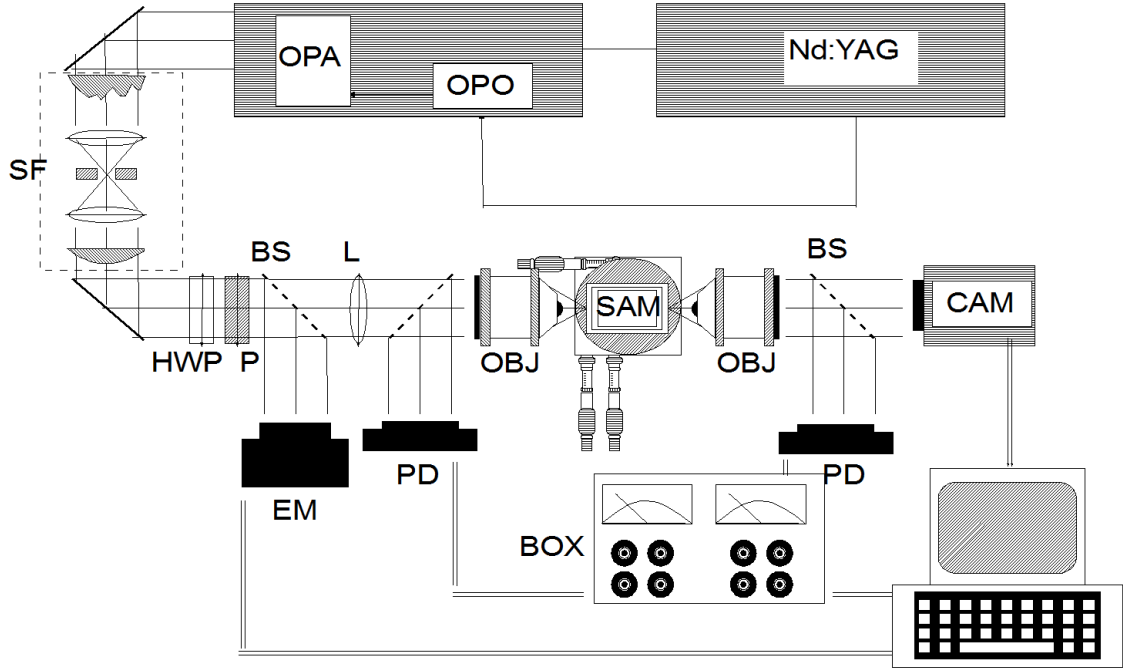


Figure 0.1: General Setup.

pulses coming from a picosecond Nd:YAG laser at $1.064\mu\text{m}$, 50mJ peak energy, 25 ps pulse-width and 10 Hz repetition-rate. These last two features minimize the detrimental effects of photorefractive damage [5] in ferroelectric crystals. The OPA/OPO output is tunable in the ranges $0.72\text{--}1.064$ and $1.064\text{--}2.1\mu\text{m}$ for idler and signal beams, respectively. Remarkably, this source produces nearly transform limited pulses with a linewidth $\sim 2\text{cm}^{-1}$ at 1550nm . Fig. 0.1 is a sketch of the typical experimental setup. The beam used in the experiments was “cleaned up” through a spatial filter (SF) in order to produce a TEM_{00} spot; polarization and power were controlled with a half-wave plate (HW) and a polarizer (P) and/or with neutral density filters; some of the beam energy was spilled out with a beam splitter (BS) and measured with either a piezoelectric energy meter (EM) or a photodetector (PD) connected to a boxcar averager (BOX). Appropriate lenses (L, OBJ) were used to shape the beam at the entrance of the sample under study (SAM) and the input coupling was controlled by micropositioners and piezoelectric stages. The light reflected and transmitted by the sample was measured with photodetectors connected to the boxcar averager or imaged with a high sensitivity ccd/vidicon camera (CAM) for visible and infrared wavelengths, respectively. Energy meter, boxcar averager and cameras were interfaced with a computer. The computer programs developed in a Labview platform were used to automatically collect and average single shot data.

Chapter 1

In situ tuning of a colloidal opal with picosecond pulses

Photonic Crystals (PC) are structures which possess a periodic high-contrast refractive index, with period of the order of the optical wavelength, in one two or three spatial dimensions[3, 6]. These structures can exhibit a photonic band-gap (PBG), i. e. they can forbid light propagation in certain directions at specific wavelengths. PC-based structures can therefore enhance confinement, guiding, filtering, switching [7–10] and -generally- processing of light and its interaction with matter, including lasing and non-linear effects [11–15]. In a scenario where several PC-elements are integrated to perform various signal-processing functions, fine adjustment and control of the individual PBGs and their resonance is essential to the operation of these novel generations of optoelectronic chips. Resonance tuning of a PBG can be pursued by acting either on the PC lattice periodicity or on the refractive index of the material. The latter approach does not require any structural change; hence, it is more suitable for control after integration, in particular when a template is infiltrated with photo-active materials. Liquid crystals [16], ferroelectrics [17] and electrochemically controlled materials [18] have been explored with this aim, applying external voltages or temperature to modify their susceptibility. In this Chapter I report on the use of picosecond pulses for tuning the PBG wavelength of polystyrene opals doped with gold nanoparticles (Au-np). By exploiting the Au-np plasmonic resonance in the visible, fine and controllable PBG tuning in selected areas of the composite PC is demonstrated, with resulting resonance shifts as large as 30 nm in the near-infrared around $1.7\mu m$. The effect, at variance with previous results on transient perturbations, consists of a permanent blue shift of the Bragg resonance associated to a decrease of the refractive index. The phenomenon is attributed to absorption induced reshaping of the Au-np embedded in the interstices, with a shift controlled by the cumulative energy irradiated on the sample at 532 nm. As the photonic crystal retains its lattice structure after laser tuning, PC's can be effectively integrated in photonic chips, as their PBG can be finely photo-adjusted in selected areas with picosecond pulses, even after realization and /or during test procedures.

1.1 Au-np doped polystyrene opal

A simple and representative example of PC is a multilayer stack, consisting of periodically alternating layers of materials with different refractive indices: a structure of this sort is the well known Bragg mirror [3, 6]. Let us consider a beam of wavelength λ orthogonally incident on the Bragg mirror and let us focus on the reflections of two interfaces, separated by a multiple of the period D . When the optical path difference between these two reflections is a multiple of λ (i.e. $m\lambda = 2Dn_{eff}$ with m an integer and n_{eff} the average refractive index) they interfere constructively. The energy of the incident wave is reflected and its forward propagation in the structure is forbidden. The forbidden wavelength is named Bragg wavelength.

A 3D PC is based on the same principle. An opal consisting in closely packed spheres possesses a face centered cubic (fcc) structure (Fig. 1.1(a)): taking into account the periodicity $D_{i,j,k}$, of the structure along a crystallographic direction $[i, j, k]$ the resonant wavelength can be expressed by an approximated formula:

$$\lambda_B = 2D_{i,j,k} \sqrt{n_{eff}^2 - \sin^2(\theta)} \quad (1.1)$$

for a beam impinging at an angle θ and with the effective refractive index $n_{eff} = \sqrt{\epsilon_{eff}}$ defined by:

$$\frac{\epsilon_{eff} - 1}{\epsilon_{eff} + 2} = f \frac{\epsilon_{sp} - 1}{\epsilon_{sp} + 2} + (1 - f) \frac{\epsilon_i - 1}{\epsilon_i + 2} \quad (1.2)$$

ϵ_{sp} and ϵ_i are the dielectric constants of the spheres and the interstices respectively and f is ratio of the volume occupied by the spheres on total volume[3].

Artificial opals are an intriguing playground to explore resonance tuning. The sample used in this work is a colloidal opal grown with polystyrene spheres at the department of Chemistry and Industrial Chemistry at University of Genoa, by Comoretto and coworkers. Opal can be prepared with a cheap technology, named the meniscus technique based on self-assembly of the colloidal spheres, allowing a fine control of the sample thickness. The growth starts with a glass substrate is partially immersed in a water suspension of polystyrene microspheres, and (Fig. 1.1(b)). A meniscus region is formed between the liquid surface and the glass substrate due to wetting by the solution; evaporation of the solvent leads to a constant solution influx, which draws colloids into the area of film formation. During the solvent evaporation these colloids experience interparticle capillary forces which organize them into close-packed arrays. The resulting opal has a fcc structure oriented in the $[111]$ direction.

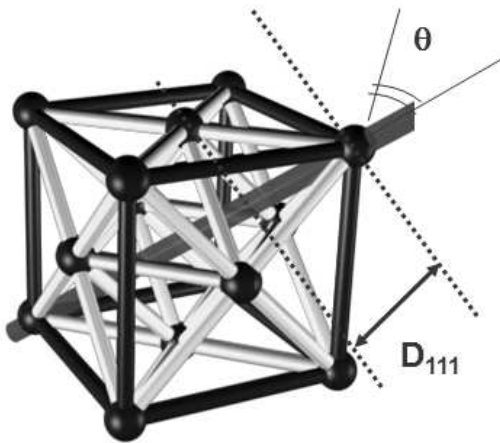
The infiltrated opals are directly grown starting from a mixed suspension of polystyrene spheres and Au-np [19, 20]. Au-np are prepared by laser ablation in water

with sodium dodecyl benzene sulfonate as a surfactant and their radius distribution around 4 nm was controlled to a standard deviation $< 50\%$ [19, 21, 22]. The resulting opal has some AuNp infiltrated in the interstices. As the spectral position of the PBG reflectivity-peak is a function of the sphere size and the Au-np doping, composite PC's were prepared with polystyrene sphere diameters from 260 to 700 nm in order to span Bragg wavelengths from visible to near infrared[3, 6, 19].

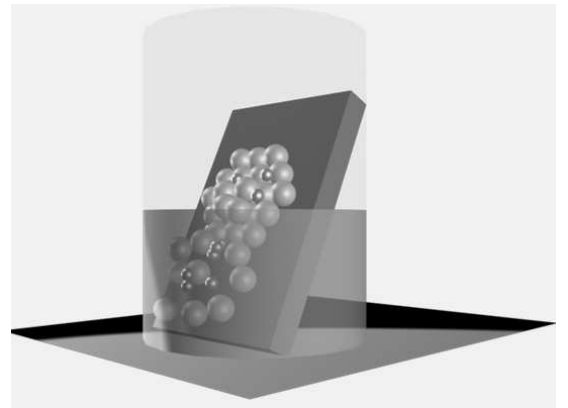
Fig. 1.2 summarizes the properties of the Au-np-infiltrated opal used in the experiments, with polystyrene spheres of diameter $a=700\text{nm}$. Fig. 1.2(a) is a scanning electron micrograph of the sample surface showing the typical packing of the PS microspheres. Fig. 1.2(b) is the measured reflectance around the Bragg resonance λ_B near $1.7\mu\text{m}$. From the dispersion of λ_B versus angle of incidence θ displayed in Fig. 1.2(c), the effective refractive index n_{eff} could be extrapolated using the Bragg-Snell expression for the stop band diffracted $[1,1,1]$ planes in the fcc structures (1.1), obtaining $n_{eff} = 1.52$. The latter value is remarkably higher than in bare opals ($n_{eff} = 1.4$) owing to infiltration [19]. The background in the spectrum Fig 1.2(b) shows the interference fringes due to multiple reflections in the sample, witnessing its good optical properties. The fringes were used to determine the sample thickness ($d = 6.5\mu\text{m}$), corresponding to about 11 layers of spheres.

1.2 Experiments and data reduction

Experiments were carried out by irradiating the opal in given locations with a fixed number (1280) of pump pulses at 532 nm, varying the energy/pulse from 18 to $115\mu\text{J}$ (fluency from 4.5 to $30 \cdot 10^{-3}\text{Jcm}^{-2}$) in steps of approximately $9\mu\text{J}$. The source used is



(a) Fcc lattice and $D_{1,1,1}$ direction



(b) Scheme for the growth of a colloidal infiltrates growth

Figure 1.1: Colloidal Opals: a face centered cubic photonic crystal

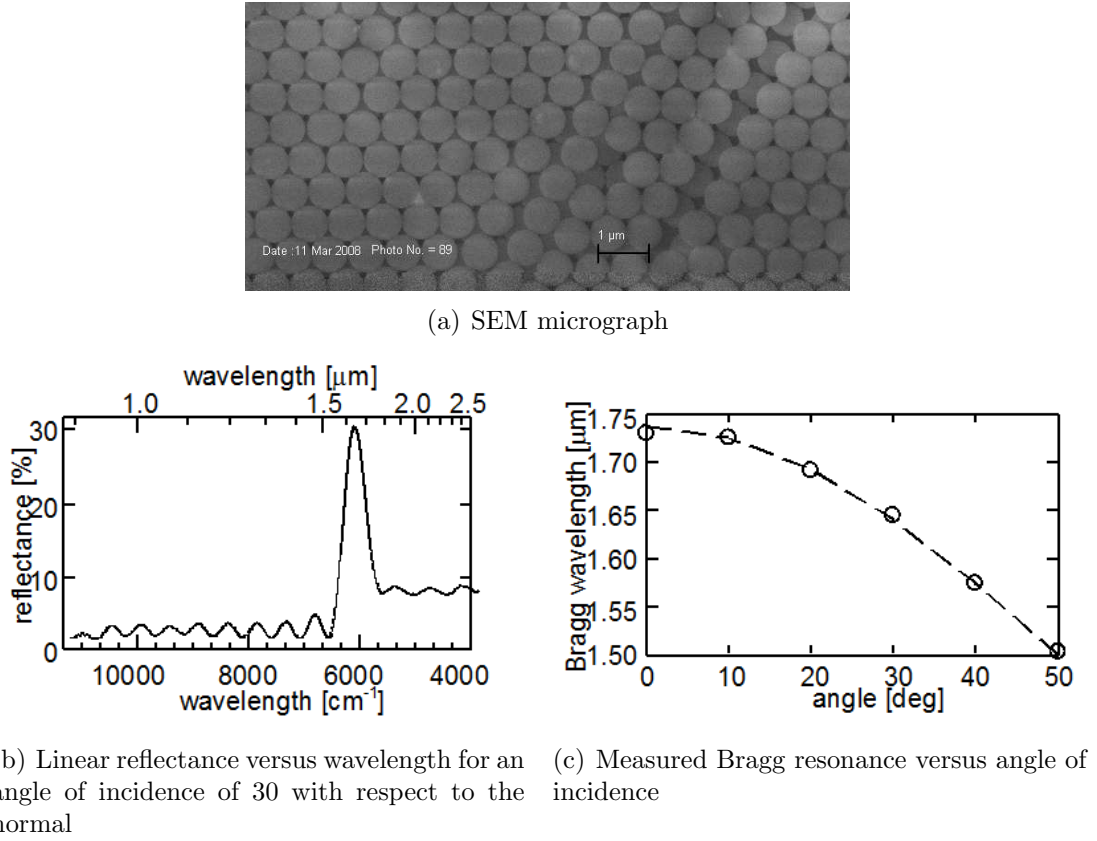
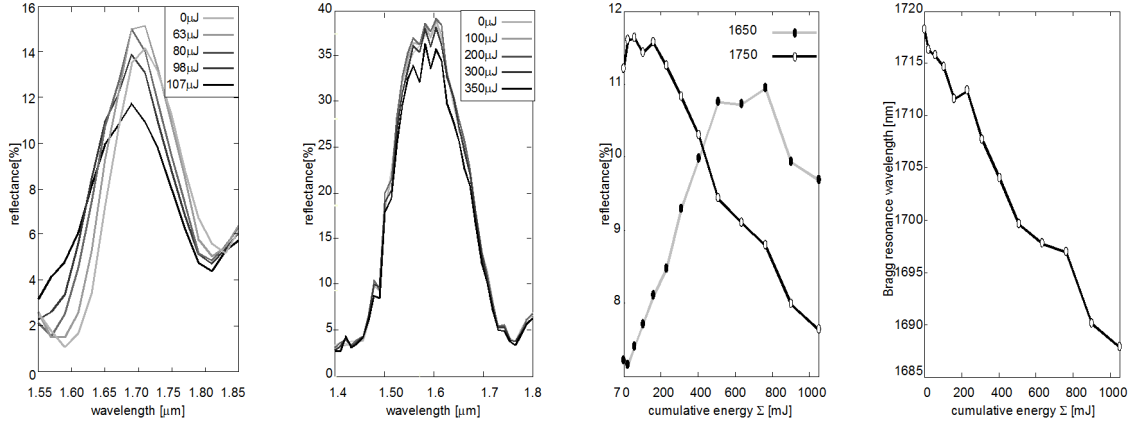


Figure 1.2: Au-np infiltrated opal with $a=700\text{nm}$ spheres

the single pulse line of the doubled laser Nd:YAG described in Fig. (0.1). PBG peak in reflectance versus the cumulative energy Σ not exceeding 1.0J (fluency $\leq 260\text{Jcm}^{-2}$) was measured. Fig. 1.3(a) displays a few representative scans and shows a blue shift of the PBG, with Bragg tuning by as much as 30nm . The absence of shift in bare samples (see Fig. 1.3(b)), even when irradiated with higher energies, shows that the observed tuning is due to the infiltrated Au-np. Fig. 1.3(c) graphs the photo-induced shift in reflectance corresponding to the PBG upper (1650 nm) and lower (1750 nm) edges versus cumulative energy. As the PBG tuning could be revealed by a probe scan well after pump illumination, the results underline the permanent nature of the effect, with a resonance shift substantially linked to the overall pump energy Σ damped into the sample.

This is clearly visible in Fig. 1.3(d) displaying the Bragg shift versus irradiation. Since the measurements were carried out by varying the energy per pulse, the substantially linear trend with indicates that the latter rules the tuning with a rate of $\approx 30\text{nm}/\text{J}$, although for $\Sigma > 0.75\text{J}$ (fluency $\leq 200\text{Jcm}^{-2}$) the Bragg peak gets smeared out by a permanent damage. The decrease in Bragg wavelength indicates an energy-dependent reduction of the effective index n_{eff} due to Au-np; a rough estimate from



(a) Scans from an Au-np opal: scans after irradiation for 1280 pump pulses with energy increasing from 18 to $115\mu J$ in $9\mu J$ steps and maximum cumulative energy of $1.0J$. (b) Scans of a bare opal PBG: scans after irradiation for 3200 pump pulses of energy from 50 to $350\mu J$ in $50\mu J$ steps and maximum cumulative energy of $4.5J$. (c) Reflectivity versus total pump energy when probing near the pump energy lower (dots) or upper (circles) band-edges (d) PBG peak Bragg wavelength versus total cumulative energy

Figure 1.3: Results from spectral scans of reflection from bare and infiltrated with Au-np opals

expression (1.1) and $n_{eff} = n_{eff}^0 + \gamma\Sigma$ yields an overall reduction $n_{eff}^0 - n_{eff} \approx 0.025$ with $\gamma \approx -25 \cdot 10^{-3} J^{-1}$.

In order to better understand the role of laser excitation at 532 nm, i. e. over the plasmon absorption of the Au-np, the scanning electron microscopy of the sample were performed in both irradiated and pristine areas, in Genoa. In particular, the irradiated areas investigated are those exposed to maximum energies of 1.0 (experimental results discussed above) and 0.6 J, the latter below the value causing a reduction in reflectance. The areas irradiated by 1.0 J show a modified morphology with some melted spheres; nonetheless the average lattice of the photonic crystal is not destroyed, as the PBG could still be revealed. No differences can be detected, however, between pristine and irradiated areas for $\Sigma < 0.6J$, consistently with the measurements above (Fig. 1.3(a)-(c)) after the use of $98\mu J$ pulses. These results confirm that the observed effects rest on Au-np infiltration and their absorption. To ascertain the role of gold (in terms of atoms or np) on the PBG tuning, using the energy dispersive x-ray spectroscopy (EDS) probe the Au content was determined (Fig. 1.4(c)) in both illuminated (with $\Sigma = 0.6J$, dashed) and pristine areas (undashed). Clearly, the Au concentration does not vary with position, thus ruling out the hypothesis of a selective laser ablation of Au atoms. The dielectric properties of the system were probed by optical spectroscopy in the visible region of Au-np plasmon absorption. After dissolving portions of the opal with toluene in order to remove the PGB structure while retaining the Au-np, the average absorbance spectra for pristine and irradiated areas ($\Sigma = 0.6J$) were acquired, as displayed in Fig.

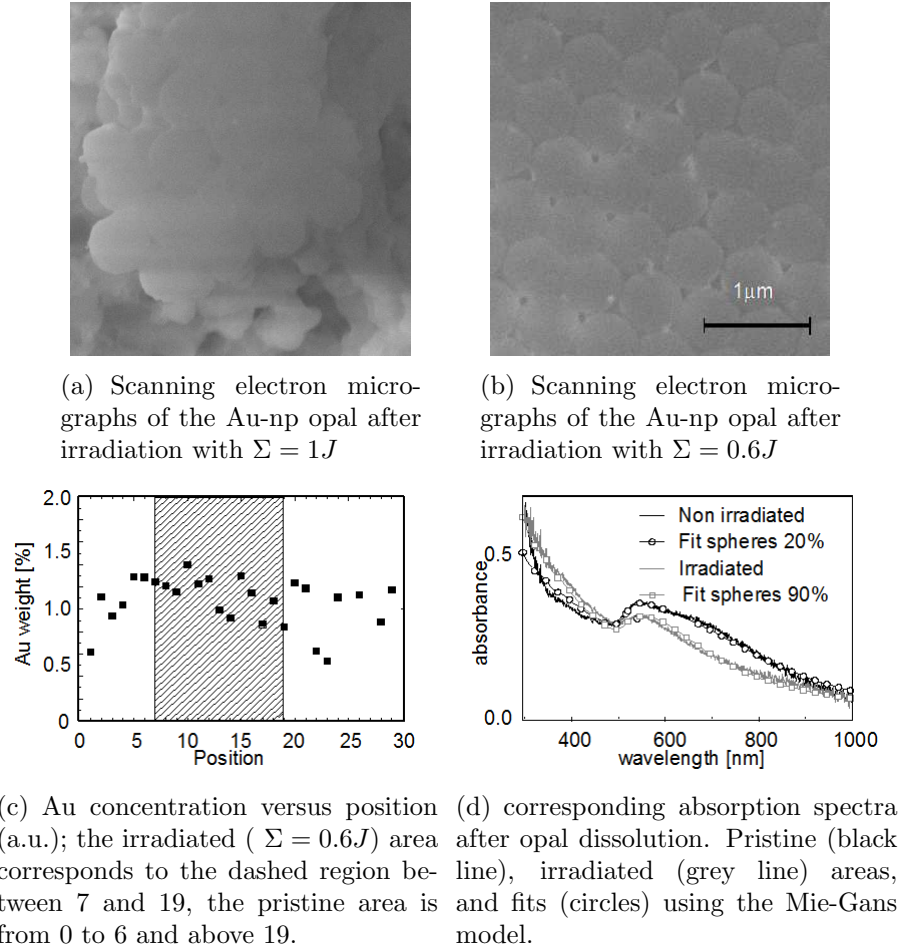


Figure 1.4: Analysis of the irradiated sample

1.4(d). In pristine areas the spectrum is typical of absorption from both spherical and spheroidal (aggregated) nanoparticles [21, 22], being the plasmon resonance close to 530 nm the signature of the former, and the 680nm shoulder extending in the NIR the signature of the latter [19, 20]. The role of spherical Au-np is detected in the spectrum of the irradiated area: a fit from the Mie-Gans model [21, 22] performed by the group of Meneghetti of University of Padua indicates that in pristine areas 80% of Au-np are aggregated, while in irradiated spots this reduces to 10%. These results unambiguously prove that the observed photobleaching for $\Sigma = 0.6J$ is due to Au-np reshaping. The distortion in irradiated absorbance is consistent with the observed reduction of the effective index n_{eff} .

1.3 Conclusion

In conclusion, a colloidal photonic crystals infiltrated with Au nanoparticles can be permanently and spatially-selectively tuned in Bragg resonance by irradiation with a ps pulsed beam at 532nm. The photo-induced effect is related to a reshaping of Au-np, which in turn reduces the effective index of the PC and results in a blue shift of the Bragg reflectivity. A tuning in excess of 30nm was obtained, finely controllable with the cumulative energy damped in the structure. The adjustable PBG of Au-np doped polystyrene opals is promising for PC-based photonic circuits for wavelength division multiplexing and optical processing.

Chapter 2

Transverse Nonlinear Optics in Heavy Metal Oxide Glasses

Nonlinear glasses (NG) have been extensively studied in the past years[23, 24]. Heavy Metal Oxides (HMOs) in particular are very promising material for ultrafast photonic due to their high optical transmittance and large linear (> 2) and ultrafast Kerr refractive indices[23–25]. Bright spatial solitons are one of the most investigated phenomena of nonlinear optics, demonstrated in media with different physical mechanism for their ubiquitous nature[26–29]. Nevertheless, solitary propagation in NGs has been restricted in a few cases. As understood and demonstrated in the first studies of light self-focusing [2, 30], spatial solitons in intensity-dependent refractive index material are stable only in planar (1D+1) system, while in (2D+1) self-confined beams undergo catastrophic collapse: additional mechanism, such as index saturation and non locality, are required for their propagation[26, 28, 31]. Self confined propagation in NGs is then reported only for femtosecond pulsed beams in the presence of multiphoton ionization [32, 33], for cw excitation in self-focusing thermo-optic systems with a diffusive nonlocality [34] and in photorefractive [35]. The lack of a glass for ultrafast self-confined propagation is enhanced by the great development in the last years of soliton based devices for all-optical processing application[36–42]. Multiphoton absorption (MPA), often present when high peak powers are employed, can play a remarkable role in nonlinear optics and in the stabilization of self-confined beams in bulk [43–49].

Like solitons, modulation instability (MI) also stems from the combined effect of nonlinearity and diffraction. Because of MI, small amplitude and phase perturbations (due to noise) grow rapidly and, as a result, a broad and homogeneous beam tends to disintegrate in propagation and break up into localized filaments, eventually generating an array of solitons [27, 29, 50–52].

In this Chapter nonlinear propagation in $Nb_2O_5 - PbO - GeO_2$ glass, fabricated at the *Laser Processing Group* of Madrid, is reported, from catastrophic collapse and transverse modulational instability at $1.064\mu m$ to single and multiple spatial solitons in the presence of MPA at $0.82\mu m$. The experiments were carried out with picosecond pulses using both circular and elliptical transverse excitations over a set of propagation distances and energies.

2.1 Self-confined beam and catastrophic collapse

A beam propagating in a Kerr medium experiences a modification of refractive index proportionally to its intensity: $n = n_o + n_2 I(\mathbf{r})$, with n_2 the Kerr coefficient.

When n_2 is positive, a beam with a gaussian profile induces a focusing lens in the medium. Being I_o the peak intensity and W_o the beam waist, the focal plane of the nonlinear lens is located in z_{sf} , which can be evaluated using with the Fermat's principle: at z_{sf} the optical path of a ray propagating in the center of the beam ($z_{sf}(n_o + n_2 I_o)$) must be equal to the optical path of a marginal ray converging into the focus with an angle θ_{sf} ($n_o z_{sf} / \cos(\theta_{sf})$), i.e. $\theta_{sf} \approx \sqrt{2n_2 I_o / n_o}$. When this angle matches the diffraction angle $\theta_d \propto \lambda / W_o$, the beam propagates in a self-guided fashion, i.e. it is a spatial soliton. This balances occurs at a critical power $P_{CR} = \lambda^2 / 2\pi n_o n_2$. The latter relation is completely independent on the geometric beam parameters: for a power exceeding P_{CR} by a small amount, self-focusing dominates over diffraction and the beam collapses: the solitary wave propagation is unstable. Nonlinear absorption, by acting on the portion of the beam at higher intensities, can prevent catastrophic collapse by reducing the focusing power of the nonlinear lens. A more rigorous treatment of laser beam propagation in optical dielectrics with a Kerr response and dissipation can be derived from a Nonlinear Schroedinger Equation (2.1) corrected for (multiphoton) absorption,

$$2ik\partial u_z + \nabla_{\perp}^2 u + \frac{n_2 k^2}{\eta_0} |u|^2 u + ik\alpha_K \left(\frac{n_0}{2\eta_0}\right)^{K-1} |u|^{2K-2} u = 0 \quad (2.1)$$

with A being the slowly varying amplitude of the electric field

$\mathcal{E}(x, y, z, t) = \frac{1}{2} u(x, y, z, t) e^{(ikz - i\omega t)} + cc.$, k the wavenumber, η_0 the vacuum impedance. α_K is the coefficient of K-photon absorption as defined by $\partial I_z = -\alpha_K I^K$. For the numerics I employed a (2D+1) beam propagator with a standard Crank-Nicolson scheme and Gaussian spatio-temporal excitation. [53]

2.2 Material Properties and Experimental Setup

HMO are characterized by phonon energies significantly lower than in silicate and borate glasses, although slightly higher than fluoride and chalcogenide systems; they are transparent and maintain good mechanical properties over a wide interval of wavelengths from the visible up to the mid-IR ($7 - 8\mu m$) [23, 24].

HMO glasses $25Nb_2O_5 - 25PbO - 50GeO_2$ mol% (nominal composition) were obtained by mixing high-purity reagents and employing standard melting procedures. The mixture was prepared in a platinum crucible and kept in a furnace at temperatures of $1100 - 1300^\circ C$ for one hour and then poured on a brass plate; this was followed by thermal annealing for one hour at $450^\circ C$ and by slow cooling to room temperature at $1.5^\circ C/min$. The resulting material was a transparent glass with a yellowish appearance

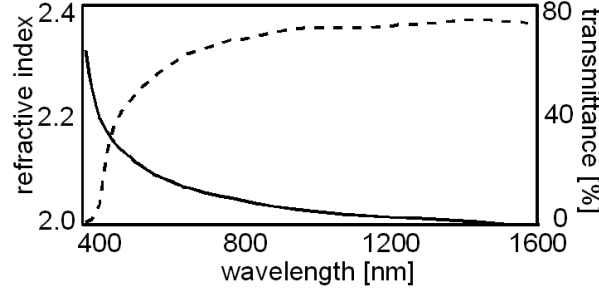


Figure 2.1: Refractive index (solid line) and linear transmittance (corrected for Fresnel losses) (dashed line) of NPG versus wavelength, as obtained by spectroscopic ellipsometry

at the eye. The glass was subsequently cut in blocks with parallel faces and polished to optical grade. HMO transmittance and refractive index were determined by spectroscopic ellipsometry [54], as graphed in Fig. 2.1 after correction for reflection (Fresnel) losses.

For the nonlinear characterization, a HMO sample of dimensions $5.7 \times 8.7 \times 11.5 \text{ mm}$ was placed in front of the pulsed beam as described in section 0.1. A 35mm-lens was used to in-couple circularly symmetric beams for soliton excitation, whereas a pair of cylindrical lenses with focal lengths $f=15$ and $f=100 \text{ mm}$, respectively, was employed to shape the elongated (elliptical) input for the study of modulational instability. Images of the output beam were collected by an infrared-enhanced CCD camera through a microscope objective, while calibrated semiconductor photodiodes measured input and transmitted power/energy with the aid of beam splitters.

2.2.1 Self-focusing and Spatial Solitons

When excited in the nonlinear regime at 1064 nm with a beam of waist $18 \mu\text{m}$, the HMO glass behaved as a purely Kerr medium and exhibited self-focusing. Although the output spot-size decreased with excitation (Fig.2.2), spatial solitons of size comparable to the input waist were not observed and, for pulse energies of $16 \mu\text{J}$ and beyond, the beam collapsed and damaged the sample, visually resulting in a small and faint central spot surrounded by an annular ring as in the inset of Fig. 2.2. Such an output profile could also be imaged by launching a low-power beam in the damaged region of the sample, confirming the permanent character of the effect. The damage and its dynamics can be ascribed to plasma-induced avalanche-breakdown for self-focused picosecond pulses in bulk solids [55, 56]. Specifically in HMO glasses, catastrophic self focusing involves a collateral stress-induced material densification (bright halo region in the inset) due to the high pressure generated in the collapsing region [57]. In order to evaluate the nonlinear refractive index I numerically fitted the data on output beam size (full width at half maximum, FWHM) versus energy by solving eq. 2.1 with $\alpha_K = 0$, obtaining $n_2 =$

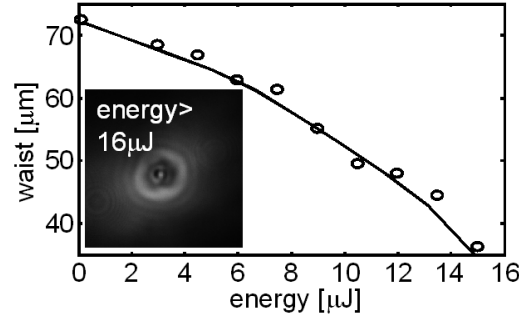


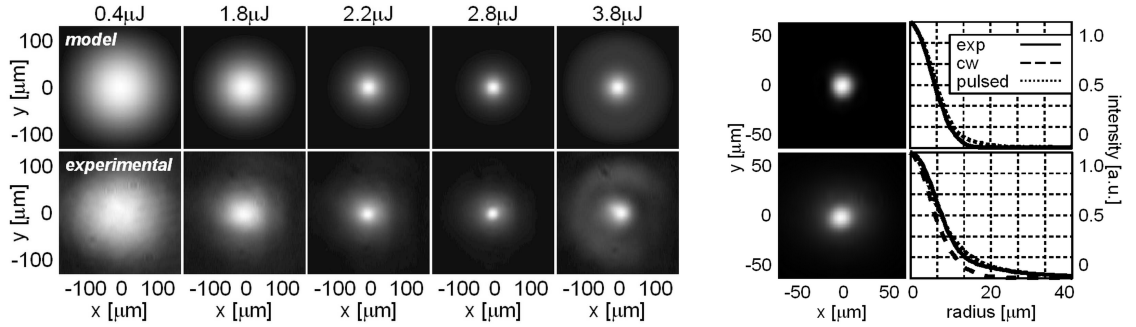
Figure 2.2: Measured (circle) and numerically evaluated beam size versus input energy for pulses at $\lambda = 1064nm$. The inset shows a case of optical damage induced by pulses of energy $> 16\mu J$.

$1.6 \times 10^{-15} cm^2/W$, corresponding to a critical power $P_{CR} = \lambda^2/2\pi n_0 n_2 \approx 560KW$ [58]; Fig. 2.2 graphs both measured and evaluated output waist (FWHM) versus excitation.

Conversely, at a wavelength of $820nm$ a beam of waist $11\mu m$ could be launched at the input and collected at the output of the sample after propagating for $5.7mm$. In this case, the output beam size (i.e. diffraction) decreased with excitation up to $2.8\mu J$, i.e. peak powers of $100kW$, eventually generating a fundamental spatial soliton (solitary wave), as visible in Fig.2.3(a). For excitations higher than $2.8\mu J$, a ring could be observed around the central spot (see rightmost panel in the bottom row of Fig. 2.3(a)). The latter is reminiscent of the transformation of a Gaussian into a Bessel beam in the presence of nonlinear losses [44]. Furthermore, at variance with previous observations at $1.064\mu m$, the sample did not undergo any damage for energies as high as $5.4\mu J$, as verified by launching a weak probe. (Damage at the input facet was ascertained by microscope inspection for inputs $> 5.4\mu J$.) The different behavior at 1.064 and $0.82\mu m$ could be interpreted in terms of multiphoton absorption, as suggested by Fig. 2.4(c), where the measured transmittance of an $11\mu m$ beam is plotted versus pulse energy for propagation over a length of $11.2mm$. The data, normalized to the linear transmittance (which accounts for Fresnel reflection), exhibit a progressive throughput reduction before permanent damage occurs. Fig. 2.3(b) shows intensity profiles at the input and after propagation for $5.7mm$ (6 Rayleigh lengths).

Owing to the use of picosecond pulses, higher-order dynamics such as group velocity dispersion and plasma-induced defocusing can be neglected. Plasma formation in self-confined propagation of ps pulses, in fact, would be accompanied by breakdown, as reported in fused silica [55, 56]: once the plasma density is high enough to arrest self-focusing (about $10^{18} cm^{-3}$ [56]), strong avalanche ionization takes place with an amplified electron density up to the damage concentration ($> 10^{19} cm^{-3}$) [59, 60]. With femtosecond pulses, conversely, their short duration prevents avalanche multiplication and allows self-trapping without collapse [32].

Two and three-photon energies in bulk HMO at $\lambda = 820nm$ are close to 3.02 and $4.54eV$, respectively. However, due to the mixed valence states, the glass sample does



(a) Calculated (top) and observed (bottom) output profiles of an $11\mu\text{m}$ Gaussian beam at $\lambda = 820\text{nm}$ propagating for 5.7mm in HMO. The fitting parameters are $n_2 = 5.5 \times 10^{-15}\text{cm}^2/\text{W}$ and $\alpha_3 = 3 \times 10^{-4}\text{cm}^3/\text{GW}^2$.

(b) (Top) Input and (bottom) output beam profiles for a propagation length of 5.7mm and input energy $2.8\mu\text{J}$: photos (left) and graphs of the radial intensity (right, thick lines). The dotted (dashed) lines are calculated radial profiles of the output intensity after integration over time (for cw excitation at the peak value).

Figure 2.3: Self-confinement at 820nm .

not exhibit a sharp cut-off in transmittance, as in other HMO glasses [61]. For this reason the evaluation of energy gap and Urbach tail [62] can be affected by a significant error; hence, the leading contribution of nonlinear absorption was identified with numerical simulations. A summary of the fits with 2PA or 3PA is presented in Fig. 2.4. Consistently with the dispersion due to the blue-ultraviolet resonance [63], the extrapolated Kerr coefficient $n_2 = 5.5 \times 10^{-15}\text{cm}^2/\text{W}$ at 820nm is higher than at 1064nm . Fig. 2.4 shows the experimental results and those calculated with the inclusion of 2PA (panel (a)) or 3PA (panel (b)) for the output beam waist versus input energy after propagation over 5.7mm . Although a point wise interpolation could be obtained using 2PA at given powers, the 3PA term in eq. (2.1) allows to fit also the transmittance curve (Fig. 2.4(c)) and to reproduce the experimental trend in a noncritical fashion, as displayed in Fig. 2.4(d). Here the calculated maximum peak intensity in the whole beam propagation is reported for pure kerr case without K-photon absorption (dotted line), in 2PA case (dashed lines) and 3PA case (continuous lines). These data are obtained integrating eq. (2.1) taking into account the peak power of the temporal profile and are normalized to the input peak intensity. In the diffracting dominating regime (below the soliton threshold $2.8\mu\text{J}$) the function is unitary for the normalization; at $2.8\mu\text{J}$ the maximum peak intensity is at the output section and the function value is comparable in 2PA and 3PA case; above $2.8\mu\text{J}$ the beam minimum waist falls inside the sample, moving towards the entrance at growing energies: the asymptotic grow of the peak intensity in the 2PA case for energies $> 2.8\mu\text{J}$ demonstrates the model instability, not supporting the absence of damage experimentally observed. Only the 3PA model counteracts the beam collapse in the whole excitation range, obtaining the best fit of the data for $\alpha_3 = 3 \times 10^{-4}\text{cm}^3/\text{GW}^2$.

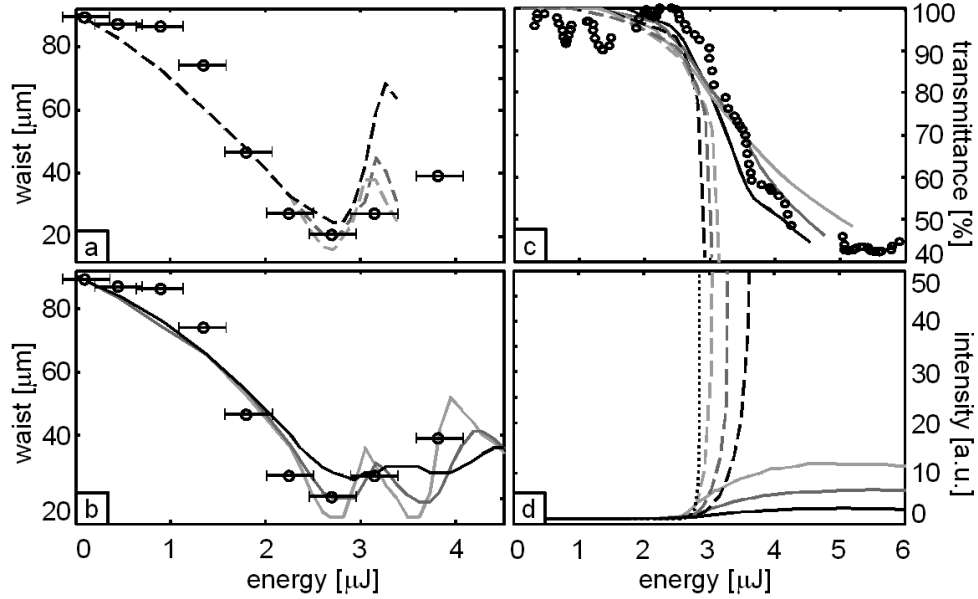


Figure 2.4: Summary of experimental results and numerical evaluation for an $11\mu\text{m}$ circular input at $\lambda = 820\text{nm}$. a-b): output beam waist (FWHM) versus excitation energy for propagation over 5.7mm . Data (open circles) and calculation for a Kerr coefficient $n_2 = 5.5 \times 10^{-15}\text{cm}^2/\text{W}$ in the presence of either (a) 2-photon absorption (2PA, dashed lines) or (b) 3-photon absorption (3PA, solid lines), time integrating the Gaussian profile. Darker lines refer to higher nonlinear absorption coefficients, which are respectively $1.2, 1.8, 2.4 \times 10^{-2}\text{cm}/\text{GW}$ for 2PA and $1.5, 3.0, 7 \times 10^{-4}\text{cm}^3/\text{GW}^2$ for 3PA. Best fits are obtained for $\alpha_2 = 1.8 \times 10^{-2}\text{cm}/\text{GW}$ and $\alpha_3 = 3 \times 10^{-4}\text{cm}^3/\text{GW}^2$ in the two cases. c) Beam transmission through an 11.2mm sample versus input energy: experimental (open circles) and calculated data in the presence of 2PA (dashed lines) and 3PA (solid lines), time integrating the Gaussian profile. The best fit is obtained considering 3PA with $\alpha_3 = 3 \times 10^{-4}\text{cm}^3/\text{GW}^2$. d) Computed peak intensity (normalized to the input) versus excitation for pure Kerr (dotted black line) with no K-photon absorption, Kerr with 2PA (dashed lines) and Kerr with 3PA (solid lines), using the coefficients and the gray scale above: only when accounting for 3PA the model counteracts collapse in the whole excitation range.

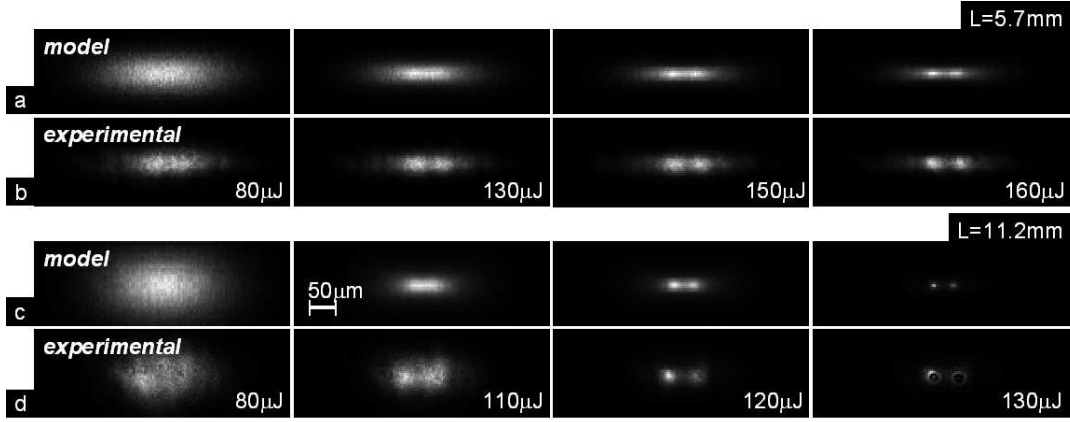


Figure 2.5: Propagation of an elliptically shaped beam launched at $\lambda = 1064nm$ with size $15\mu m \times 215\mu m$: output profiles for propagation lengths of (a-b) $5.7mm$ and (c-d) $11.2mm$; (b) and (d) are the experimental results, (a) and (c) are numerical simulations with $n_2 = 1.6 \times 10^{-15} cm^2/W$.

2.2.2 Modulation Instability and Multiple Filamentation

Modulation Instability (MI) is a precursor of individual and multiple soliton formation [27, 29]: the interplay between nonlinearity and diffraction can break-up a homogeneous beam into localized filaments, eventually generating an array of solitons [50–52]. The unstable behavior observed at $1064nm$ was confirmed by investigating MI of a beam of size $15\mu m \times 215\mu m$ injected at the input of the HMO sample. By letting the beam propagate through the three distinct lengths available in our glass block, the formation of filaments along the major axis of the ellipse was recorded, with patterns determined by both input position and propagation distance. Consistently with the theory [50], even when the number of filaments changed owing to a localized perturbation (i.e., launching the beam at a specific input location), for a given excitation energy the spacing between filaments was conserved, as shown in Fig. 2.6. Filaments catastrophically collapsed for energies higher than $160\mu J$ when propagating through the shortest sample section and than $130\mu J$ through the longest one. Simulations performed with the model used for propagation at $1064nm$, adding white noise (10% of beam amplitude) to the input field result in good agreement with the experimental data, as shown in Fig. 2.5.

Although 3PA plays the role of stabilizing mechanism for spatial solitons at $820nm$, it necessarily shortens the useful length for self-trapped propagation. This limitation can be mitigated by a surrounding energy background, the latter able to ‘refill’ the energy lost by the beam(s) [44, 64]. I numerically investigated such nonlinear space dynamics in those conditions under which MI and multiple filamentation were observed in HMO. The resulting evolution pattern, presented in Fig. 2.7(a), suggests that the propagating filaments undergo complex phenomena such as multiple focusing (breathing) with conical emission from the foci and additional filament generation from the released energy [65, 66]. The beam was launched from the left and superimposed to a white

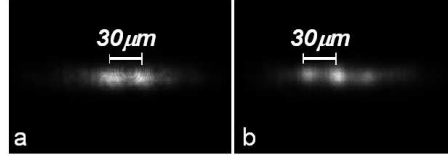


Figure 2.6: Output intensity distribution for an elliptically shaped beam propagating through 5.7mm at $\lambda = 1064\text{nm}$. The sample was excited with 0.14mJ per pulse and spot size $15\mu\text{m} \times 215\mu\text{m}$ in two distinct locations at the entrance facet: either two or three filaments were generated with a separation of $30\mu\text{m}$.

noise pattern to permit the (numerical) development of MI [50]. Fig. 2.7(b) shows the energy evolution (dashed line) and the corresponding maximum transverse peak intensity (solid line) versus z : the peak value increases by more than one order of magnitude with respect to the initial sections where filaments are yet to be formed. The energy trend demonstrates that the role of nonlinear absorption becomes more appreciable (i.e. steeper decrease vs z) once self-focusing comes into play. Most filament energy is released after collapse into "spatial" (as compared to spatio-temporal) conical emission, as previously observed also in other non dissipative media [65, 67, 68], notwithstanding the role of multiphoton losses in transforming the Gaussian excitation into a Bessel-like beam [44, 64, 69]. Finally, the radiated energy could seed a successive generation of filaments as in Ref. [65].

In the experiments an elliptically shaped Gaussian beam of dimensions $13.5\mu\text{m} \times 130\mu\text{m}$ was focused at the input facet of the HMO sample; at variance with the 1064nm excitation, the generated filaments did not undergo collapse or damage but their number increased with input energy, in agreement with the predictions from standard treatments of transverse modulational instability [50]. Fig. 2.8(b) shows the output intensity profiles

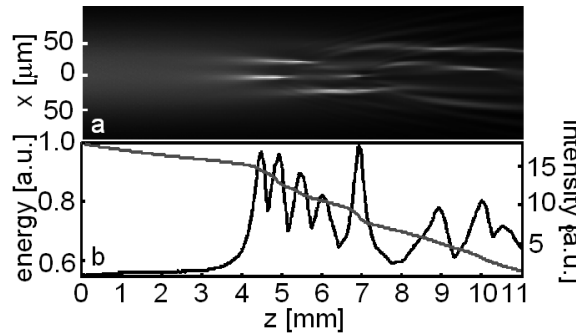


Figure 2.7: (a) Intensity distribution calculated in the plane xz for an elliptical beam at 820nm launched with size $13.5\mu\text{m} \times 130\mu\text{m}$ with energy $24\mu\text{J}$ assuming $n_2 = 5.5 \times 10^{-15}\text{cm}^2/\text{W}$ and $\alpha_3 = 3 \times 10^{-4}\text{cm}^3/\text{GW}^2$. As it propagates from left to right, the beam undergoes multiple filamentation with conical emission, refocusing as well as formation of new filaments. b) Input-normalized energy (dashed line) and maximum transverse intensity (solid line) versus propagation

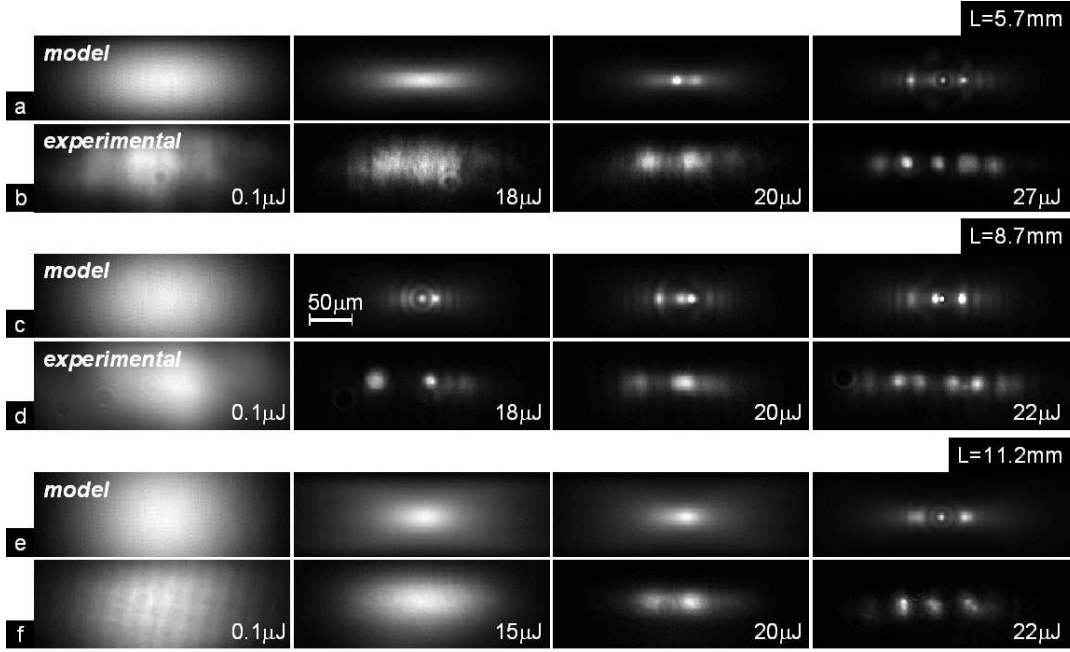


Figure 2.8: (a) Calculated and b) acquired output cross-sections of elliptic beams launched at $\lambda = 820nm$ with size $13.5\mu m \times 130\mu m$ after propagation over $5.7mm$. c) and d): as a) and b) but for input size $13.5\mu m \times 130\mu m$ and propagation over $8.7mm$. e) and f): as a) and b) but for input size $13.5\mu m \times 180\mu m$ and propagation over $11.2mm$. In the numerics I used $n_2 = 5.5 \times 10^{-15} cm^2/W$ and $\alpha_3 = 3 \times 10^{-4} cm^3/GW^2$.

after propagation for $5.7mm$: two and five filaments were formed at 20 and $27\mu J$, respectively. In the latter case, small rings appeared around the beam axes owing to energy release via conical emission (details in Fig. 2.9(a)). Moreover, consistently with their predicted evolution (Fig. 2.7), the filaments exhibited various sizes and intensities due to maximum self-focusing at different propagation distances. The calculated profiles (Fig. 2.8(a)), obtained with the actual input parameters, are in remarkable agreement with the observed dynamics: self-focusing at low energies, break-up and splitting in two filaments, conical emission etc. even though their transverse shape and locations depend on the specific realization of a process (MI and multiple filamentation) which is seeded

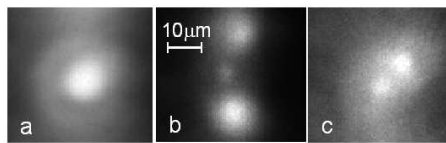


Figure 2.9: Details on the filamentation of elliptic beams at $\lambda = 820nm$: (a) for input energy of $27\mu J$ and propagation through a distance of $5.7mm$; (b) energy $22\mu J$ and distance $8.7mm$; (c) energy $22\mu J$ and distance $11.2mm$.

by noise. While the inclusion of 3PA allowed us to reproduce with remarkable fidelity the observed behavior even for longer propagation distances (e.g. 8.7 and 11.2mm, Fig. 2.8(c-d) and Fig. 2.8 (e-f), respectively), no agreement was found with the experimental results when excluding 3PA from the model (eq. (2.1)) and accounting for 2PA only. This further confirms that three-photon absorption is the leading dissipative mechanism at 820nm and the one responsible for soliton stabilization in this HMO.

2.3 Conclusions

In conclusion, in this chapter I presented a thorough investigating on the nonlinear response of a novel heavy-metal-oxide glass of the ternary system $Nb_2O_5GeO_2PbO$ when spatially self-focusing ps beams in the near infrared. The results, interpreted with the aid of a nonlinear Schroedinger equation corrected for multiphoton absorption, indicate that the glass has a purely Kerr response around 1064nm, whereas three-photon absorption plays a significant role around 820nm. At the latter wavelength 3PA prevents catastrophic collapse and allows the formation of stable spatial solitary waves, even when originated from a wide beam through modulational instability. Complex dynamics such as conical emission and multiple filamentation were observed and numerically reproduced, confirming the Kerr-like nature of the HMO response. This HMO glass appears to be an excellent candidate for self-confined propagation in ultrafast dielectrics.

Chapter 3

Guided-wave Second Harmonic Generation in Surface Periodically Poled Ferroelectrics

Despite their extensive use and numerous applications in quasi-phase-matched (QPM) parametric interactions, Lithium Niobate (LN) and Lithium Tantalate (LT) remain among the most investigated dielectrics for harmonic generation (HG)[70, 71]. Several techniques have been developed for periodic poling based on their ferroelectric properties, including electric-field poling [72]. In addition, processes for waveguide fabrication in LN have been mastered, the most successful being those based on Titanium in-diffusion and proton exchange (PE)[73]. Recently, aiming at the realization of shorter and shorter domain lengths for QPM-SHG at smaller wavelengths [74] as well as counter-propagating wave mixing [75–78], Surface Periodic Poling (SPP) was introduced by Busacca *et al.* to better control mark-to-space ratios [74, 79, 80]. SPP relies on *overpoling* a ferroelectric substrate, with domain spreading and merging beneath the patterned photoresist layer, thus creating a complete ferroelectric inversion with the exception of relatively shallow unpoled domains at the LN surface under the pattern.

This chapter summarizes the progresses of the SPP-PE technique for second harmonic generation (SHG), from the first waveguides realized in LN for 1550nm frequency doubling but suffering of limited ferroelectric domain depth, to the most recent samples in LT for UV generation with a remarkable conversion efficiency of $7.5\%W^{-1}cm^{-2}$.

3.1 Surface periodically poled for frequency doubling

Non-centrosymmetric materials exhibit a quadratic dependence of the polarization from the electric field \mathcal{E} , $\mathcal{P} = \epsilon_o n^2 \mathcal{E} + 2\epsilon_o d \mathcal{E}^2$, with ϵ_o vacuum permittivity and d the quadratic strength. The latter relation rules the mixing of three waves with different frequency, i.e., in the frame of a quantum-mechanical description, it permits three photons of different energies to interact. In an SHG process, two photons from the fundamental frequency

wave (FF) and energy $\hbar\omega$ can annihilate into a photon of energy $\hbar\omega/\pi$, generating the second harmonic (SH) of the original frequency. An efficient conversion process takes place when the total momentum of the interacting particles is also conserved. Due to material dispersion, the latter occurrence is not generally satisfied [81]. QPM is a popular method to phase match FF and SH and consists in creating a nonlinear lattice in the material. When properly chosen, the momentum of the induced grating can compensate the momentum mismatch of the interacting particles, helping the conversion [82].

In ferroelectric crystals like LN and LT a periodic sign change of the nonlinear coefficient d can be achieved through the reversal of the spontaneous polarization, thus creating different “domains” alternating periodically with a given sign of d . SPP is a technique for QPM based on electric field poling.

The samples studied in this work were fabricated by SPP at the *Centro per la Ricerca Elettronica in Sicilia* (CRES) of Monreale (Italy). $500\mu\text{m}$ thick z-cut substrates of congruent LN/LT were spin-coated with photoresist and UV exposed to define a proper periodic pattern on the “-z” surface by standard photolithography. Then the samples were electric-field poled using high voltage pulses to overcome the coercive field. For waveguide fabrication, poled substrate were initially coated with a SiO_2 layer, where channel openings - from 1 to $7\mu\text{m}$ in width - were defined by standard photolithography and wet-etching in HF. Proton exchange was then carried out by the so-called sealed-ampoule method [83] in a solution of benzoic acid (BA) and lithium benzoate (LB). This yielded low proton concentration (α phase [84]) channel waveguides supporting TM modes. The compatibility between SPP and PE was verified by chemically etching the samples and using scanning electron microscopy. Fig. 3.1(a) is a micrograph of a typical QPM channel after etching in HF.

3.2 Frequency doubling in SPP LN waveguides @1550nm

The first batch of SPP-PE waveguides, designed for SHG from a 1550nm pump with a QPM period of $16.8\mu\text{m}$, was characterized by a limited depth of the non-inverted domains. The sample was studied experimentally with the setup described in section 0.1. The OPO source was focused with a 20x microscope objective at the channel input with circular beams of waist $w_0 \approx 3.6\mu\text{m}$. The output FF and SH profiles were imaged with Vidicon and Si-CCD cameras, respectively, using a 63x microscope objective (see Fig. 3.1(b)). Energy and peak power were measured with Ge and Si photodiodes. All measurements were taken at room temperature with the aid of a Peltier cell and a temperature controller.

SHG measurements were conducted either at a fixed wavelength by varying the FF input power or by scanning the FF wavelength, ratioing the second-harmonic output to the fundamental input to obtain the conversion efficiency. Typical results versus FF wavelength are shown in Fig. 3.2(a) for an FF peak power of 2kW: even though the

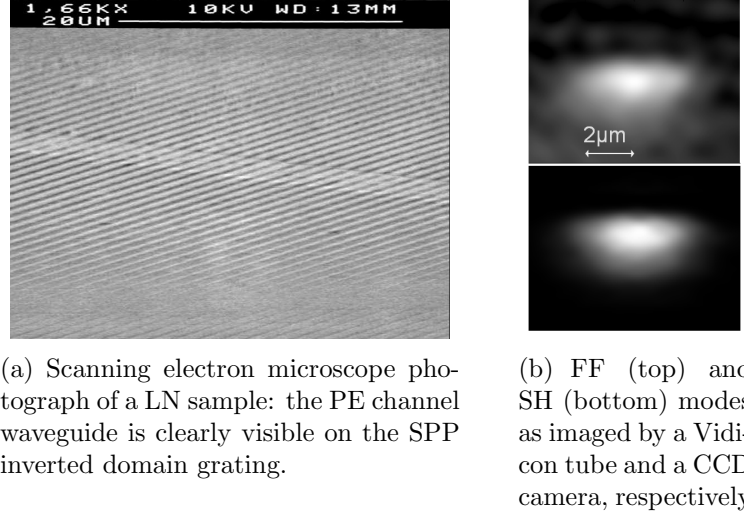


Figure 3.1: LN sample for 1550nm frequency doubling

data (symbols) are plotted versus wavelength rather than detuning, the sinc-like shape is in substantial agreement with the expected one for CW excitation (solid line). The full width at half maximum is about 1nm, yielding an effective QPM grating length of 1cm, corresponding to the overall sample length. Despite the low efficiency, the latter result confirmed the good uniformity of the PE poled sample in both QPM periodicity and waveguide parameters [82].

By repeating the SHG scan at higher peak powers the wavelength of maximum conversion (the FF resonance wavelength for SHG) shifted with excitation, as visible in Fig. 3.2(b).

Light propagation and QPM in only a *partially* inverted medium can have detrimental effects on SH generation and produce a nonlinear phase shift due to cascading under phase-mismatch [85, 86]. Therefore, in order to quantitatively interpret the experimental data, not only the periodically poled transverse region providing first-order QPM must be taken into account, but also the homogeneously inverted portion of the waveguides extending below the actual domains. The SH generated in this region is not expected to alter the peak conversion efficiency, since it is phase mismatched; however, it can play an important role on the phase coherently accumulated by the FF in propagation, therefore on the peak wavelength of maximum conversion [85, 87, 88].

For monochromatic first-order TM-polarized guided-wave modes at FF and SH, the electric field E of an x -propagating eigenmode is:

$$\mathcal{E}_u(x, y, z, t) = \frac{1}{2}u(x, t)\tilde{e}_u(y, z)\exp[i(\omega_u t - k_u x)] + c.c., \quad (3.1)$$

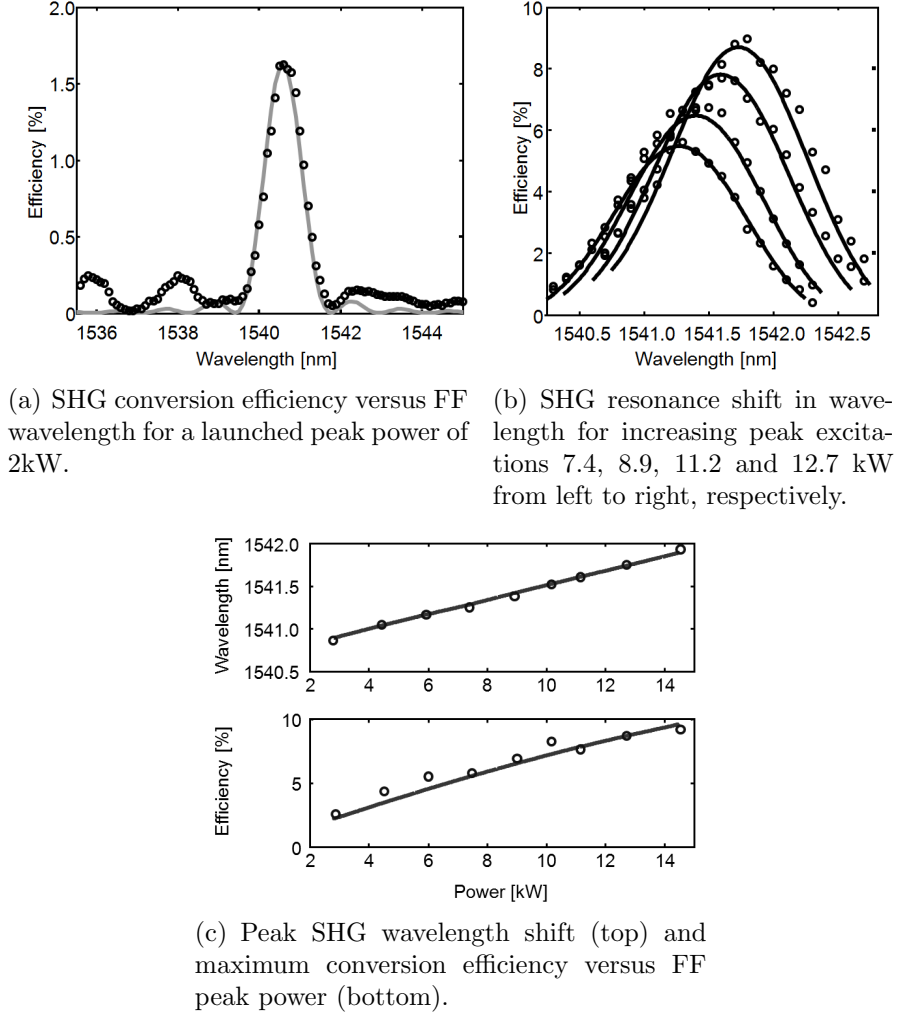


Figure 3.2: Measurement of frequency doubling in LN sample. The experimental values (open circles) are numerically interpolated using Eq. (3.2) (solid curves).

where $u(x, t)$ is the slowly varying amplitude (in space and time) measured in \sqrt{W} , $(|u(x, t)|^2)$ is the optical power of the mode, $\tilde{e}_u(y, z)$ is the transverse profile measured in $\sqrt{\Omega}/m$ and k_u is the guided wave propagation-constant.

In the presence of a rectangular QPM grating with limited-depth inverted domains and an intrinsic third-order response, assuming a negligible contribution from higher-order modes at SH (non quasi-phase-matched to the FF mode), the coupled-mode equations for SHG take the form:

$$\begin{aligned}
 \partial_x u + \frac{\partial_t u}{c_u} &= -u^* w [\chi_1 \exp(-i\Delta k_1 x) + i\chi_2 \exp(-i\Delta k_2 x)] \\
 &\quad - in_2 \frac{2\pi}{\lambda_{FF}} (f_{uu} |u|^2 + 2f_{uw} |w|^2) u - \frac{\alpha_u}{2}, \\
 \partial_x w + \frac{\partial_t w}{c_w} &= u^2 [\chi_1 \exp(i\Delta k_1 x) - i\chi_2 \exp(i\Delta k_2 x)] \\
 &\quad - in_2 \frac{4\pi}{\lambda_{FF}} (2f_{uw} |u|^2 + f_{ww} |w|^2) w - \frac{\alpha_w}{2},
 \end{aligned} \tag{3.2}$$

being $u(x, t)$ and $w(x, t)$ the amplitudes of FF and SH waves, respectively, c_u and c_w (α_u and α_w) the group velocities (linear absorption coefficients) at FF and SH, respectively, and n_2 the non-resonant Kerr coefficient [89]. The third-order nonlinear effects, i.e. self and cross-phase modulation, are weighed by the overlap integrals[81]

$$f_{jk} \equiv \frac{\int \int_{-\infty}^{+\infty} |e_j(y, z)|^2 |e_k(y, z)|^2 dydz}{\int \int_{-\infty}^{+\infty} |e_j(y, z)|^2 dydz \int \int_{-\infty}^{+\infty} |e_k(y, z)|^2 dydz} \quad (j, k = u, w) \tag{3.3}$$

As visible, the contributions from poled and unpoled regions of the waveguide are distinct [90]. χ_2 and $\Delta k_2 = k_w - 2k_u$ are the nonlinear coefficient and the mismatch in the unpoled region, respectively, while χ_1 and $\Delta k_1 = \Delta k_2 - G$ are the corresponding ones in the poled region, being $G = 2\pi/\Lambda$ the first-order wave vector contribution of the QPM grating with period Λ . The nonlinear coefficients can be expressed as

$$\chi_i = d_{eff_i} \gamma_i \sqrt{\frac{8\pi^2 \eta_0 f_{SHG}}{\lambda_{FF}^2 N_u^2 N_w}}, \quad (i = 1, 2) \tag{3.4}$$

with overlap integral.

$$f_{SHG} \equiv \frac{\left[\int \int_{-\infty}^{+\infty} e_w^*(y, z) e_u^2(y, z) dydz \right]^2}{\left[\int \int_{-\infty}^{+\infty} |e_u(y, z)|^2 dydz \right]^2 \int \int_{-\infty}^{+\infty} |e_w(y, z)|^2 dydz}. \tag{3.5}$$

with $d_{eff_1} = 2d_{33}/\pi$, $d_{eff_2} = d_{33}$, and γ_i parameters accounting for the waveguide cross-section:

$$\begin{aligned}\gamma_1 &= \frac{\int_{-\infty}^{+\infty} \int_{Z_0}^{+\infty} e_w^*(y, z) e_u^2(y, z) dy dz}{\int_{-\infty}^{+\infty} \int_{-\infty}^{+\infty} e_w^*(y, z) e_u^2(y, z) dy dz}, \\ \gamma_2 &= \frac{\int_{-\infty}^{+\infty} \int_{-\infty}^{Z_0} e_w^*(y, z) e_u^2(y, z) dy dz}{\int_{-\infty}^{+\infty} \int_{-\infty}^{+\infty} e_w^*(y, z) e_u^2(y, z) dy dz} = 1 - \gamma_1,\end{aligned}\tag{3.6}$$

with Z_0 delimiting the domain depth h .

Eqs. (3.2) model SHG in a partially poled QPM sample. They were solved numerically, assuming a Gaussian profile for the FF pulses, a propagation length $L=1\text{cm}$, propagation losses $\alpha_u = \alpha_w = 0.2\text{cm}^{-1}$ at both wavelengths (accounting for both the α -phase and the domain inversion [91, 92]) and an input coupling efficiency equal to 73% and consistent with the measured throughput of 60%. The overlap integrals were calculated from the acquired intensity distributions (Fig. 3.1(b)), resulting in effective areas $1/f_{uu} = 52.99\mu\text{m}^2$ and $1/f_{ww} = 23.11\mu\text{m}^2$ for FF and SH self-phase modulation, respectively, $1/f_{uw} = 44.08\mu\text{m}^2$ for cross-phase modulation and $1/f_{SHG} = 76.68\mu\text{m}^2$ for SHG. Since both cubic and quadratic terms contribute to the shift (3.17), the Kerr coefficients previously measured by independent methods and reported in literature were adopted to estimate the pertinent QPM quantities, i.e. the nonlinearity d_{33} and the constant γ_1 related to the depth h of the domains. The depth was extracted from γ_1 using a modal solver. The index profile along z was reconstructed from the experimental data (Fig. 3.1(b)).

A graph of the domain depth and of d_{33} versus the n_2 coefficient is shown in Fig. 3.3. The largest value of $n_2 \approx 10 \times 10^{-20}\text{m}^2/\text{W}$ [63] provided $\gamma_1 = 0.0104$, corresponding to $d_{33} = 16.5\text{pm}/\text{V}$ and $h \approx 440\text{nm}$. Conversely, the smallest reported $n_2 \approx 5 \times 10^{-20}\text{m}^2/\text{W}$ gave $\gamma_1 = 0.0095$, corresponding to $d_{33} = 18\text{pm}/\text{V}$ and $h \approx 430\text{nm}$. Therefore, while the domain depth was marginally affected by the size of n_2 , the quadratic response appeared lower than previously reported [82]. Noticeably, by neglecting the third-

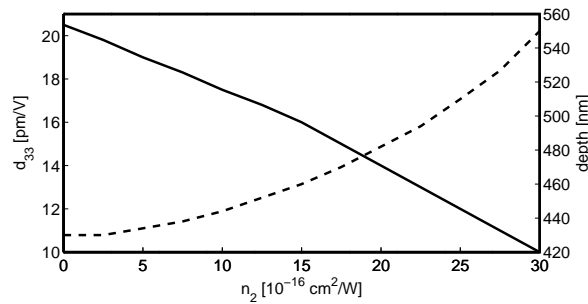


Figure 3.3: Quadratic nonlinear coefficient d_{33} (solid line) and domain depth (dashed line) obtained from data interpolation at variance of the Kerr coefficient n_2

order nonlinearity altogether (but keeping the propagation losses) we got $\gamma_1 = 0.0088$, with $d_{33} = 19.5 \text{ pm/V}$ and $h \approx 420 \text{ nm}$. These results are perfectly consistent with the expression (3.17). Moreover, the found nonlinear values are in good agreement with $d_{33} = 19.5 \text{ pm/V}$ as measured at $1.313 \mu\text{m}$ [93].

An interesting reduction of Eqs. (3.2), showing the role of the cascaded and Kerr contribution can be obtained from the simplified system, neglecting absorption and temporal walk-off as well as the cubic terms depending on the SH field [94, 95],

$$\begin{aligned}\partial_x u(x, \tau) &= -u^* w [\chi_1 \exp(-i\Delta k_1 x) + i\chi_2 \exp(-i\Delta k_2 x)] + \\ &\quad -in_2 \frac{2\pi}{\lambda_{FF}} f_{uu} |u|^2 u, \\ \partial_x w(x, \tau) &= u^2 [\chi_1 \exp(i\Delta k_1 x) - i\chi_2 \exp(i\Delta k_2 x)] + \\ &\quad -in_2 \frac{8\pi}{\lambda_{FF}} f_{wu} |u|^2 w,\end{aligned}\tag{3.7}$$

having introduced $\tau = t - x/c_u$.
 Defining $|u|^2 = u(0)^2 g(\tau)^2$ for the input power in $x = 0$ and U , W and $\Delta\kappa_i$ as in the expressions

$$\begin{aligned}U &= u \exp \left[-i \frac{2\pi}{\lambda_{FF}} n_2 f_{uu} u(0)^2 g(\tau)^2 x \right], \\ W &= w \exp \left[-i \frac{8\pi}{\lambda_{FF}} n_2 f_{wu} u(0)^2 g(\tau)^2 x \right],\end{aligned}\tag{3.8}$$

$$\Delta\kappa_i = \Delta k_i + \frac{4\pi}{\lambda_{FF}} n_2 u(0)^2 g(\tau)^2 (2f_{uw} - f_{uu}) \quad (i = 1, 2),\tag{3.9}$$

the coupled-mode equations for $U(x, \tau)$ and $W(x, \tau)$ take the form

$$\partial_x U = -U^* W [\chi_1 \exp(-i\Delta\kappa_1 x) + i\chi_2 \exp(-i\Delta\kappa_2 x)]\tag{3.10}$$

$$\partial_x W = U^2 [\chi_1 \exp(i\Delta\kappa_1 x) - i\chi_2 \exp(i\Delta\kappa_2 x)].\tag{3.11}$$

Finally, since $\Delta\kappa_2 \gg \Delta\kappa_1$ ($\Delta k_1 \approx 0$) and $\chi_2 \gg \chi_1$, neglecting the rapidly oscillating term $\sin[(\Delta\kappa_2 - \Delta\kappa_1)x]$, Eq. (3.11) reduces to

$$\partial_{xx} U + i\Delta\kappa_2 \partial_x U \cong -\chi_2^2 (|U|^2 - |W|^2) U.\tag{3.12}$$

In the small conversion limit ($|W|^2 \ll |U|^2$), after defining the FF phase ϕ as in $U = u(0)g(\tau) \exp(-i\phi)$ with $g(\tau)$ the FF temporal profile, Eq. (3.12) corresponds to:

$$(\partial_x \phi)^2 - \Delta\kappa_2 \partial_x \phi - \chi_2^2 w(0)^2 g(\tau)^2 \cong 0\tag{3.13}$$

that admits the solution [86]

$$\phi = -\frac{\Delta\kappa_2 x}{2} \left(\sqrt{1 + \frac{4\chi_2^2 u(0)^2 g(\tau)^2}{(\Delta\kappa_2)^2}} - 1 \right) \approx -\frac{\chi_2^2 u(0)^2 g(\tau)^2}{\Delta\kappa_2} x, \quad (3.14)$$

because for low powers $u(0)^2 \ll \Delta\kappa_2/\chi_2^2$ and, in the same limit, $\Delta\kappa_2 \gg (8\pi/\lambda_{FF})n_2 f_{uw} u(0)^2$, $(4\pi/\lambda_{FF})n_2 f_{uu} u(0)^2$ (and so $\Delta\kappa_2 \approx \Delta\kappa_2$). The cascading contribution is self-defocusing [85–88, 96–98]. The SH power at the output of the sample (of length L) is

$$|w|^2 = |W|^2 = \chi_1^2 u(0)^4 g(\tau)^4 L^2 \text{sinc}^2 \left[(\Delta\kappa_1 + \Delta C u(0)^2 g(\tau)^2) \frac{L}{2} \right], \quad (3.15)$$

where

$$\Delta C = \frac{8\pi}{\lambda_{FF}} n_2 f_{uw} - \frac{4\pi}{\lambda_{FF}} n_2 f_{uu} + \frac{2\chi_2^2}{\Delta\kappa_2}. \quad (3.16)$$

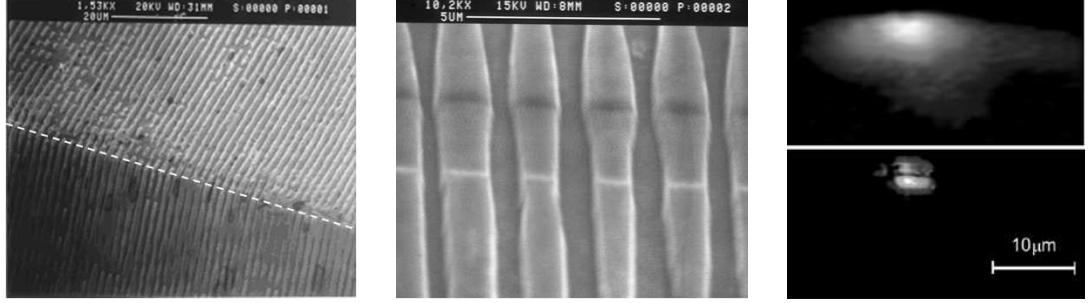
From Eq. (3.15), λ_0 for peak efficiency, i.e. the SHG resonant wavelength in the limit of zero FF power, corresponds to $\Delta\kappa_1 + \Delta C u(0)^2 g(\tau)^2 = 0$; therefore, at first order,

$$\lambda = \Delta C \frac{\lambda_0}{G} u(0)^2 g(\tau)^2 + \lambda_0. \quad (3.17)$$

Expression (3.17) is consistent with the linear trend experimentally found (Fig. 3.2(c)) for a positive ΔC ; thereby, cross-phase modulation (with a positive n_2) and cascading (with $\Delta\kappa_2 > 0$) dominate the λ shift. Since no permanent or semipermanent material effects such as hysteresis, memory, or damage could be detected, other effects (photorefractive, photovoltaic, higher order) potentially contributing to a resonance-wavelength shift were entirely negligible in the waveguides.

3.3 Ultra-Violet Generation in Periodically-Poled Lithium Tantalate Waveguides

The limitation to the efficiency of frequency doubling experienced in the previously described case was overcome by Busacca and coworkers in next generations of samples. Domains as deep as $40\mu\text{m}$ (visible in the microphotographs in Fig. 3.4(b)) were obtained in PE SPP LT guided-wave parametric generators. These LT waveguides, featuring short period QPM ($2\mu\text{m}$), are the first integrated optics coherent UV sources at 365.4 nm, with remarkable conversion efficiencies exceeding $7.5\%W^{-1}\text{cm}^{-2}$.



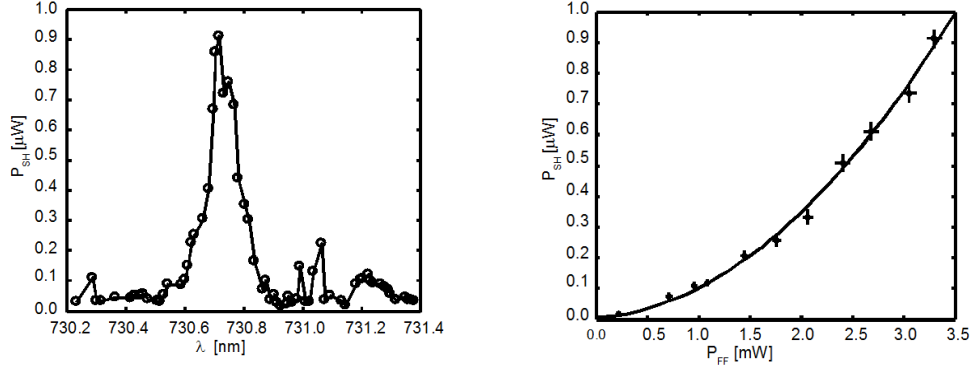
(a) Photograph of the periodic domain pattern with $2\mu\text{m}$ periodicity as revealed by chemical etching in Hydrofluoric acid; the dashed line indicates the edge of the sample with the -Z facet above it. (b) Detail of a proton exchanged channel waveguide (white trace) on the etched sample. (c) FF (top) and SH (bottom) intensities profiles at the output of a $7\mu\text{m}$ wide LT channel.

Figure 3.4: LT sample for UV generation

For the nonlinear characterization, an Ar-ion pumped Ti-Sapphire laser, tunable from 700 to 980nm and with a 40GHz line-width, was end-fired by a microscope objective into the channel waveguides, keeping the sample at a constant temperature of $250 \pm 0.1^\circ\text{C}$ in order to reduce or eliminate the chances of photorefractive damage. A filter at the waveguide output helped eliminating the fundamental frequency (FF) pump in the near-infrared while another filter suppressed the remaining Argon-ion light. The generated second-harmonic (SH) power in the UV was measured with a calibrated (Silicon) photodiode equipped with a chopper and a lock-in amplifier to reduce the noise level, while both FF and SH modal profile were imaged by a CCD camera, as shown in Fig. 3.4(c) for a 7 m-wide channel.

Fig. 3.5(a) graphs the generated SH power versus FF wavelength in $7\mu\text{m}$ -wide waveguides. The SHG resonance occurred between fundamental-order TM modes for an input wavelength close to 730.7nm . Although the PE channel was multimode in the UV and the effective refractive index of some higher-order SH modes were rather close to the TM_{00} , the latter dominated the process owing to a significantly larger overlap integral. Features in Fig 3.5 (a) are due to slight inhomogeneities in the QPM sample. The generated corresponding mode in the UV exhibited the expected quadratic growth versus FF power, as displayed in Fig. 3.5(b) for a 2cm-long channel with a 1.0cm QPM (SPP) region in the middle, equidistant from input and output facets. The values graphed in Fig. 3.5(b) are purged of the external (Fresnel reflections) losses.

Fig. 3.5(a) graphs the generated SH power versus FF wavelength in $7\mu\text{m}$ -wide waveguides. The SHG resonance occurred for an input wavelength close to 730.7nm . Although the PE channel was multimode in the UV and the effective refractive index of some higher-order SH modes were rather close to the TM_{00} , the latter dominated the process owing to a significantly larger overlap integral. The features in Fig 3.5 (a) are due



(a) SH generated power versus wavelength of the FF injected in a $7\mu m$ -wide channel. The resonance is at $\lambda_{FF} = 730.7nm$.

(b) Quadratic trend of the generated UV light versus FF input power at the QPM resonant wavelength.

Figure 3.5: UV generation in LT waveguides

to slight inhomogeneities in the QPM sample. The generated corresponding mode in the UV exhibited the expected quadratic growth versus FF power, as displayed in Fig. 3.5(b) for a 2cm-long channel with a 1.0cm QPM (SPP) region in the middle, at the same distance from input and output facets. The values graphed in Fig. 3.5(b) are purged of the external (Fresnel) reflections losses. From the SHG resonance in Fig. 3.5(a) with a $FWHM = 0.152nm$, we could estimate the effective length of the surface-poled region to exceed 9.5mm, the latter value indicating that nearly the whole poled region (10mm) contributed to the parametric process; otherwise stated, the SPP process produced a uniform QPM grating. The fitting of the experimental data in Fig. 3.5(b) was obtained with a material nonlinearity $d_{33} = 6.9pm/V$, for an effective area $1/f_{SHG} = 130\mu m^2$ as extrapolated from the modal profiles in Fig. 3.4(c). In spite of neglecting the absorption at SH and FF, the latter value is consistent with what reported by Meyn and coworkers for bulk poled crystals. [99]

3.4 Conclusions

The recent progresses of the SPP-PE technology for SHG in ferroelectrics were summarized in this Chapter. The first generation of samples, despite a good mark-to-space ratio of 50:50, was negatively affected by the small depth of the non-inverted ferroelectric domains, the latter reducing the conversion efficiency and introducing a sizable quadratic cascading. The next samples, conversely, possessed domains as deep as $40\mu m$ for QPM periods of $2\mu m$. These waveguides are the first integrated optics sources of coherent UV at 365.4 nm, with remarkable conversion efficiencies exceeding $7.5\%W^{-1}cm^{-2}$.

Chapter 4

Spatial Simultons in Quadratic Nonlinear Lattice

In analogy to Kerr spatial solitons, parametric solitons in quadratic materials are well known examples of spatial solitary waves in optics[100]. Following previous chapter, where the mechanism of the $\chi^{(2)} : \chi^{(2)}$ *cascaded* nonlinearity [85] is introduced, the interaction between the FF and the SH in a $\chi^{(2)}$ crystal can result in a net phase shift as the one occurring in $\chi^{(3)}$ media. In a broader sense than SHG cascading, the phase exchange between the waves interacting in a second order process is responsible for their “locking” in a quadratic soliton or “*simulton*”. Differently from the Kerr case, a simulton does not define a waveguide that could be probed by another signal. The first experimental works on spatial simultons appeared in 1995 (Torruellas *et al.* [101] and Schiek *et al.* [102] for the cases of bulk KTP and LN planar waveguides, respectively). The recent developments in the technology of periodically poled ferroelectrics and the extension of QPM to the bidimensional case resulted in the fabrication of 2D nonlinear lattices. This chapter is devoted to the study of simultons in these structures, with particular reference to Hexagonally poled Lithium Niobate (HexLN), used for the first experimental demonstration of simultons in 2D nonlinear lattices. The chapter is organized as follows:

- General equations will be derived for two non-collinear concurrent QPM processes defined by two reciprocal lattice vectors G_{10} and G_{01} , specifically referring to the hexagonal geometry. The general system is equivalent to SHG in a transversely periodic quadratic medium. These equations will be simplified in the undepleted SHG regime, showing that the SHG process can be viewed as the superposition of two SHG interactions in opposite directions.

- A numerical and theoretical study will address the simultons resulting from the general equations, demonstrating by the use of Lie symmetry that solitary propagation can rigorously occur only along the mid-angle between the two lattice vectors. In this regime the structure behaves as a quadratic nonlinear waveguide. A class of simultons with a large stability domain will be showed, analytically demonstrating that the stability threshold is described by the classical VK criterion.

-Using classical results of $\chi^{(2)}$ cascaded processes, a regime will be defined where the general equations support walking solitary waves, i.e. solitons that can be steered in angle depending on the excitation; this leads to the existence of two spectral regions for beam confinement and opposite lateral displacements, i.e. where the structure behaves as a wavelength controlled (nonlinear) de-multiplexer.

-Reports on the experimental demonstrations of self-confined propagation in the two regimes will follow.

4.1 Derivation of the Governing Equations

Multidimensional nonlinear lattices can allow PM with several vectors in reciprocal space. The simplest interaction involves two of them. With no loss of generality, an interesting structure is a triangular lattice with period Λ defined in the plane (X,Y) (see fig. 4.1(a)).

The periodicity in direct (real) space is completely described by the primitive vectors $\mathbf{a}_{10}, \mathbf{a}_{01}$, with $|\mathbf{a}_{10}| = |\mathbf{a}_{01}| = \Lambda$, forming an angle $\frac{2\pi}{3}$ with one another. The latter vectors are related to the primitive reciprocal vectors \mathbf{G}_{10} and \mathbf{G}_{01} through $\mathbf{a}_i \cdot \mathbf{G}_j = 2\pi\delta_{ij}$, with $|\mathbf{G}_{10}| = |\mathbf{G}_{01}| = G_o = \frac{4\pi}{\sqrt{3}\Lambda}$. When the quadratic response is modulated in sign by such a triangular lattice, it can be expanded in the Fourier series

$$\begin{aligned} d(X, Y) &= \sum_{nm} d_{nm} e^{i\mathbf{G}_{nm} \cdot \mathbf{r}}, \quad \mathbf{G}_{nm} = n\mathbf{G}_{10} + m\mathbf{G}_{01} \\ d_{n,m} &= \frac{1}{\text{CellArea}} \iint_D d(X, Y) e^{-i\mathbf{G}_{nm} \cdot \mathbf{r}} dX dY \end{aligned} \quad (4.1)$$

Since $d(X, Y)$ is a real and symmetric function, with a proper choice of the origin $d_{10} = d_{01} = d_o$ with d_o real. The reciprocal vectors can be conveniently expressed in an (x, z) system rotated by a small angle θ with respect to (X,Y) (Fig. 4.1(a)), i.e.:

$$\begin{aligned} \mathbf{G}_{10} &= G_o \left(\frac{\sqrt{3}}{2} - \frac{\theta}{2} \right) \hat{\mathbf{z}} + G_o \left(\frac{1}{2} + \frac{\theta\sqrt{3}}{2} \right) \hat{\mathbf{x}} \\ \mathbf{G}_{01} &= G_o \left(\frac{\sqrt{3}}{2} + \frac{\theta}{2} \right) \hat{\mathbf{z}} - G_o \left(\frac{1}{2} - \frac{\theta\sqrt{3}}{2} \right) \hat{\mathbf{x}} \end{aligned} \quad (4.2)$$

In the (1+1)D reference system (x, z), the coupled equations for SHG can be expressed as:

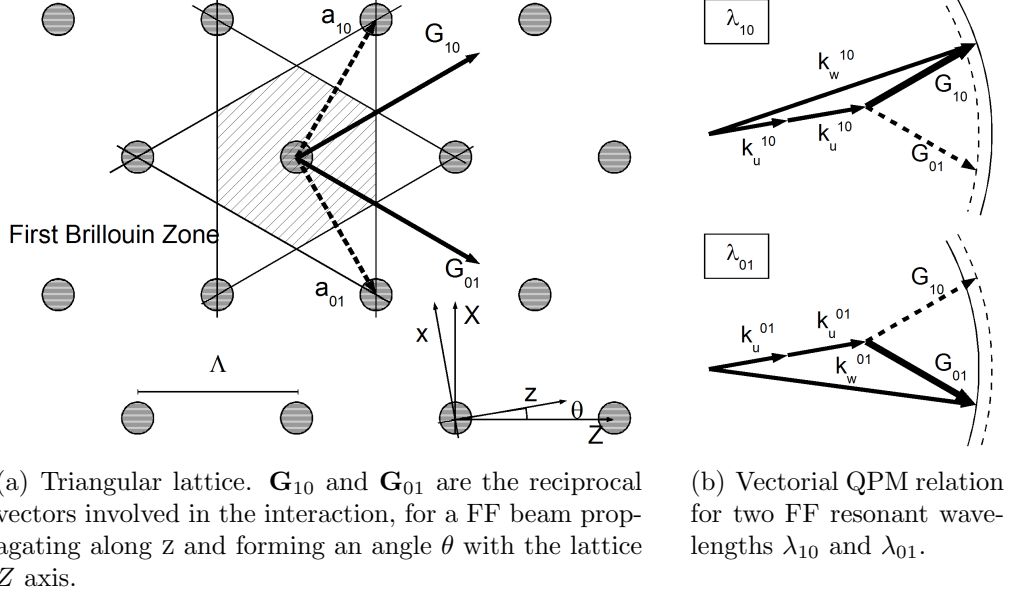


Figure 4.1: Geometry of SHG in a triangular lattice.

$$\begin{aligned}
 (\partial_{zz} + \partial_{xx})E_u + k_u^2 E_u + 4k_o^2 d(x, z) E_u^* E_w &= 0 \\
 (\partial_{zz} + \partial_{xx})E_w + k_w^2 E_w + 8k_o^2 d(x, z) E_u^2 &= 0
 \end{aligned} \tag{4.3}$$

where $k_o = \omega/c$ ($2k_o = 2\omega/c$) is the wave number of the FF (SH) in vacuum, $\mathcal{E}_u = \frac{1}{2}E_u e^{-i\omega t} + cc$ ($\mathcal{E}_w = \frac{1}{2}E_w e^{-2i\omega t} + cc$) is the electric field at FF (SH), n_u (n_w) and $k_u = n_u k_o$ ($k_w = 2n_w k_o$) are the refractive index and the wave number in the medium at FF (SH), respectively. In the case under study the quantity $k_w - 2k_u - G_o \frac{\sqrt{3}}{2}$ is small; hence, the waves are close to PM owing to the two vectors \mathbf{G}_{10} and \mathbf{G}_{01} .

4.1.1 No depletion plane-wave regime

In order to gain physical insight on multiple PM, the equations can be simplified by assuming plane-wave propagation and an FF generating a weak SH. For a plane-wave at FF launched along z and generating the superposition of two SH plane-waves:

$$\begin{aligned}\mathcal{E}_u &= \frac{1}{2}E_ue^{-i\omega t} + cc = \frac{1}{2}Ue^{i(k_uz - \omega t)} + cc \\ \mathcal{E}_w &= \frac{1}{2}E_we^{-2i\omega t} + cc = \frac{1}{2}(W_{10}(z)e^{i\mathbf{k}_w^{10} \cdot \mathbf{r}} + W_{01}(z)e^{i\mathbf{k}_w^{01} \cdot \mathbf{r}})e^{-i2\omega t} + cc\end{aligned}\quad (4.4)$$

with $|\mathbf{k}_w^{10}| = |\mathbf{k}_w^{01}| = k_w$. Under no FF depletion and paraxial approximation, the equation for the SH reduces to:

$$2i\mathbf{k}_w^{10} \cdot \hat{\mathbf{z}} W'_{10} e^{i\mathbf{k}_w^{10} \cdot \mathbf{r}} + 2i\mathbf{k}_w^{01} \cdot \hat{\mathbf{z}} W'_{01} e^{i\mathbf{k}_w^{01} \cdot \mathbf{r}} + U^2 8k_o^2 d_o (e^{i\mathbf{G}_{10} \cdot \mathbf{r} + 2k_u z} + e^{i\mathbf{G}_{01} \cdot \mathbf{r} + 2k_u z}) = 0 \quad (4.5)$$

Since W_{10} , W_{01} and U do not depend on \mathbf{x} , the solution to the above requires $\mathbf{k}_w^{10} \cdot \hat{\mathbf{x}} = \mathbf{G}_{10} \cdot \hat{\mathbf{x}}$ and $\mathbf{k}_w^{01} \cdot \hat{\mathbf{x}} = \mathbf{G}_{01} \cdot \hat{\mathbf{x}}$; hence, the equation can be re-cast in the system:

$$\begin{aligned}2i\mathbf{k}_w^{10} \cdot \hat{\mathbf{z}} W'_{10} + 8k_o^2 d_o U^2 e^{-i(\mathbf{k}_w^{10} \cdot \hat{\mathbf{z}} - 2k_u - \mathbf{G}_{10} \cdot \hat{\mathbf{z}})z} &= 0 \\ 2i\mathbf{k}_w^{01} \cdot \hat{\mathbf{z}} W'_{01} + 8k_o^2 d_o U^2 e^{-i(\mathbf{k}_w^{01} \cdot \hat{\mathbf{z}} - 2k_u - \mathbf{G}_{01} \cdot \hat{\mathbf{z}})z} &= 0\end{aligned}\quad (4.6)$$

with the vectorial QPM condition for $W_{10/01}$:

$$\begin{aligned}\mathbf{G}_{10/01} \cdot \hat{\mathbf{x}} - \mathbf{k}_w^{10/01} \cdot \hat{\mathbf{x}} &= 0 \\ \mathbf{G}_{10/01} \cdot \hat{\mathbf{z}} - \mathbf{k}_w^{10/01} \cdot \hat{\mathbf{z}} + 2\mathbf{k}_u \cdot \hat{\mathbf{z}} &= 0\end{aligned}\quad (4.7)$$

The first of (4.7) defines the transverse components of the vectors $\mathbf{k}_w^{10/01}$, i.e. the propagation angle of the waves $W_{10/01}$. This angle has to be small in the paraxial approximation, implying $G_o \ll k_w$, usually verified in physically relevant cases. θ introduces a correction on a small angle and can be neglected, leading to $\mathbf{k}_w^{10/01} \cdot \hat{\mathbf{x}} = \pm \frac{G_o}{2}$ and $\mathbf{k}_w^{10/01} \cdot \hat{\mathbf{z}} = \tilde{k}_w$, with $\tilde{k}_w^2 + \frac{G_o^2}{4} = k_w^2$.

Conversely, θ plays an important role in the second of (4.7). Using $G_o \ll k_w$ and $\theta \ll 1$, the second of (4.7) can be rewritten as:

$$\begin{aligned}
& \mathbf{G}_{10/01} \cdot \hat{\mathbf{z}} - \mathbf{k}_w^{10/01} \cdot \hat{\mathbf{z}} + 2\mathbf{k}_u \cdot \hat{\mathbf{z}} = \\
& \left(\frac{\sqrt{3}}{2} \mp \frac{\theta}{2}\right)G_o + 2k_u - \sqrt{k_w^2 - \frac{G_o^2}{4}(1 \pm 2\sqrt{3}\theta + o(\theta^2))} \approx \\
& \left(\frac{\sqrt{3}}{2} \mp \frac{\theta}{2}\right)G_o + 2k_u - k_w - \frac{G_o^2}{8k_w^2}(1 \pm 2\sqrt{3}\theta) \approx \\
& \left(\frac{\sqrt{3}}{2} \mp \frac{\theta}{2}\right)G_o + 2k_u - k_w - \frac{G_o^2}{8k_w^2} = \\
& \Delta k_o \mp \frac{\theta}{2}G_o
\end{aligned} \tag{4.8}$$

where Δk_o is the mismatch:

$$\Delta k_o = \frac{\sqrt{3}}{2}G_o + 2k_u - k_w - \frac{G_o^2}{8k_w^2} \approx \frac{\sqrt{3}}{2}G_o + 2k_u - k_w \tag{4.9}$$

Summarizing the above, the generated SH can be expressed as the superposition of two plane waves propagating at opposite angles with respect to the FF direction. Such angles are defined by the QPM resonance with the two reciprocal lattice vectors:

$$\begin{aligned}
\mathcal{E}_w &= \frac{1}{2}E_w e^{-2i\omega t} + cc = \frac{1}{2}W(\mathbf{x}, \mathbf{z})e^{i\tilde{k}_w \mathbf{z} - 2i\omega t} + cc \\
W(\mathbf{x}, \mathbf{z}) &= W_{10}(\mathbf{z})e^{i\frac{G_o}{2}\mathbf{x}} + W_{01}(\mathbf{z})e^{-i\frac{G_o}{2}\mathbf{x}}
\end{aligned} \tag{4.10}$$

with transverse and longitudinal SH wave-vector components such that:

$$\tilde{k}_w^2 + \frac{G_o^2}{4} = k_w^2 \tag{4.11}$$

The two SH plane waves satisfy the two separate equations

$$\begin{aligned}
2i\tilde{k}_w^{10}W'_{10} + 8k_o^2 d_o U^2 e^{i\Delta k^{10}z} &= 0 \\
2i\tilde{k}_w^{01}W'_{01} + 8k_o^2 d_o U^2 e^{i\Delta k^{01}z} &= 0
\end{aligned} \tag{4.12}$$

with the two phase mismatches

$$\Delta k_{10/01} = \Delta k_o \mp \frac{\theta}{2} G_o \quad (4.13)$$

4.1.2 General case

After describing the system in the no depletion approximation, the general case can be addressed. The fields are cast as

$$\begin{aligned} \mathcal{E}_u &= \frac{1}{2} E_u e^{-i\omega t} + cc = \frac{1}{2} U(x, z) e^{ik_u z - i\omega t} + cc \\ \mathcal{E}_w &= \frac{1}{2} E_w e^{-2i\omega t} + cc = \frac{1}{2} W(x, z) e^{i\tilde{k}_w z - i2\omega t} + cc \end{aligned} \quad (4.14)$$

The SH wavenumber is conveniently expressed as \tilde{k}_w , defined by the previous relation (4.11). In the paraxial approximation, using the definitions 4.9 with Δk_o small, Eqs. (4.3) are written in the form:

$$\begin{aligned} 2ik_u \partial_z U + \partial_{xx} U + 8k_o^2 d_o \cos\left(\frac{G_o}{2}(x - \theta z)\right) U^* W e^{-i\Delta k_o z + i\frac{\sqrt{3}}{2} G_o \theta x} &= 0 \\ 2i\tilde{k}_w \partial_z W + \partial_{xx} W + \frac{G_o^2}{4} W + 16k_o^2 d_o \cos\left(\frac{G_o}{2}(x - \theta z)\right) U^2 e^{i\Delta k_o z - i\frac{\sqrt{3}}{2} G_o \theta x} &= 0 \end{aligned} \quad (4.15)$$

As in the previous section, the term $e^{i\frac{\sqrt{3}}{2} G_o \theta x}$ can be neglected (it induces small variations on the SH phase and propagation direction as compared to $\frac{G_o^2}{4}$ and θ , respectively, as it can be verified with the substitution $W = W' e^{-i\frac{\sqrt{3}}{2} G_o \theta x}$). Owing to paraxiality, since $n_u \approx n_w$, the approximation $2i\tilde{k}_w \partial_z W \approx 2ik_w \partial_z W \approx 4ik_u \partial_z W$ is allowed.

Using the standard substitutions and normalizations

$$\begin{aligned}
X &= xx_o \\
Z &= z \, 2L_R = z \, k_u x_o^2 \\
U(X, Z) &= \frac{1}{2d_o k_o^2 x_o^2} u(x, z) \\
W(X, Z) &= \frac{1}{2d_o k_o^2 x_o^2} w(x, z) e^{i\Delta k_o z} \\
\gamma &= \frac{G_o x_o}{2} \quad \vartheta = k_u x_o \theta \\
\Delta_o &= x_o^2 k_u \Delta k_o \\
\Delta &= \Delta_o - \frac{\gamma^2}{4}
\end{aligned} \tag{4.16}$$

the system reduces to the form:

$$\begin{aligned}
i\partial_z u + \frac{\partial_{xx} u}{2} + 2 \cos(\gamma(x - \vartheta z)) u^* w &= 0 \\
i\partial_z w + \frac{\partial_{xx} w}{4} - \Delta w + 2 \cos(\gamma(x - \vartheta z)) u^2 &= 0
\end{aligned} \tag{4.17}$$

4.2 Analysis of the governing Equations

A powerful and general approach for studying differential equations is the theory of the local Lie group [103, 104]. Roughly speaking, a *variational symmetry* of an equation is a transformation in the space of dependent and independent variables that transforms a solution of the equation in another solution of the same. Each variational symmetry, through Noether's theorem, is connected to a conserved quantity of the system. Following a standard procedure, [103, 104], it is possible to find *all* the symmetries of a system. As an example, let us consider the system modeling SHG in a homogeneous material (SHG-hom), in the general case of non collinear FF and SH, with the previous convention on the fields and with Δ and ϑ the phase mismatch and the walkoff, respectively:

$$\begin{aligned}
i\partial_z u + \frac{\partial_{xx} u}{2} + u^* w &= 0 \\
i\partial_z w + \frac{\partial_{xx} w}{4} - i\vartheta w - \Delta w + u^2 &= 0
\end{aligned} \tag{4.18}$$

This system possesses three symmetries associated to the conserved quantities[100]:

i) The energy associated to phase invariance:

$$Q = Q_u + Q_w = \int |u|^2 + |w|^2 dx \quad (4.19)$$

ii) The momentum associated to translational invariance in x:

$$M = M_u + \frac{1}{2}M_w = \frac{i}{2} \int u(\partial_x u^* - u^* \partial_x u) + \frac{1}{2}(w \partial_x w^* - w^* \partial_x w) dx \quad (4.20)$$

iii) The Hamiltonian associated to translational invariance in z:

$$H = \frac{1}{2} \int |\partial_x u|^2 + \frac{|\partial_x w|^2}{4} - (u^{*2}w + u^2w^*) dx + \frac{\Delta}{2}Q_w - \frac{\vartheta}{2}M_w \quad (4.21)$$

where

$$\begin{aligned} \partial_z u &= i\delta_{u^*} H & \partial_z u^* &= -i\theta_u H \\ \partial_z w &= 2i\delta_{w^*} H & \partial_z w^* &= -2i\theta_w H \end{aligned}$$

From eqs. (4.17), since the phase invariance is preserved and therefore the energy (4.19), the translational invariances with respect to x and z are no longer independent for the presence of an explicit dependence from $(x - \theta z)$. The momentum for a solution of eqs. (4.17) is defined as eq. (4.20) and the Hamiltonian as

$$H = \frac{1}{2} \int |\partial_x u|^2 + \frac{|\partial_x w|^2}{4} - 2 \cos(\gamma(x - \theta z))(u^{*2}w + u^2w^*) dx + \frac{\Delta}{2}Q_w \quad (4.22)$$

These two quantities are no longer independent, since the translational invariance with respect to $x' = x - \theta z$ requires the conservation of the new quantity $H' = H - \theta M$.

Important simplifications can be obtained looking for a solution that preserves the symmetry of the equation. From the classification approach [103, 104], a general class of solutions for eqs. (4.18) is $u = u_o(x - cz)e^{i\beta z}$ and $w = w_o(x - cz)e^{i2\beta z}$, with β and c two free parameters[100]; hence, invariant solutions of eqs. (4.18) can propagate in *any* direction. The classification problem for eqs. (4.17) leads to solutions of the form $u = u_o(x - \theta z)e^{i\beta z}$ and $w = w_o(x - \theta z)e^{i2\beta z}$, possessing just one free parameter β . In the general case, invariant solution in propagation (solitary waves) are expected only in the direction $x' = x - z\theta$, with H' the Hamiltonian of the system. This class of solutions can be used in the ODE system derived from eqs. (4.17) with $x' = x - \theta z$, $u = u_o(x')e^{i\beta z}$ and $w = w_o(x')e^{i2\beta z}$:

$$\begin{aligned}
\frac{u_o''}{2} - i\vartheta u_o' - \beta u_o + 2 \cos(\gamma x') u_o^* w_o &= 0 \\
\frac{w_o''}{4} - i\vartheta w_o' - (\Delta + 2\beta) w_o + 2 \cos(\gamma x') u_o^2 &= 0
\end{aligned} \tag{4.23}$$

equivalent to the variational problem [100, 105] for the eigenvalue β :

$$\delta(H' + \beta Q) = 0 \tag{4.24}$$

4.2.1 Symmetric case

Let us first analyze the case $\theta = \vartheta = 0$, when the vectorial QPM condition (4.7) is symmetric:

$$\begin{aligned}
i\partial_z u_o + \frac{\partial_{xx} u_o}{2} - \beta u_o + 2 \cos(\gamma x) u_o^* w_o &= 0 \\
i\partial_z w_o + \frac{\partial_{xx} w_o}{4} - (\Delta + 2\beta) w_o + 2 \cos(\gamma x) u_o^2 &= 0
\end{aligned} \tag{4.25}$$

Eqs. (4.25) have too many independent parameters, but their number can be reduced by applying a standard transformation: [100]

$$\begin{aligned}
z &= \frac{\tilde{z}}{\beta} & x &= \frac{\tilde{x}}{\sqrt{\beta}} \\
u_o &= \beta \tilde{u} & w_o &= \beta \tilde{w} \\
\gamma &= \tilde{\gamma} \sqrt{\beta} \\
\alpha &= \frac{\Delta}{\beta} + 2 = \frac{\Delta_o}{\beta} + 2 - \frac{\tilde{\gamma}^2}{4}
\end{aligned} \tag{4.26}$$

The resulting equations can be cast in the form:

$$\begin{aligned}
i\partial_{\tilde{z}} \tilde{u}_o + \frac{\partial_{\tilde{x}\tilde{x}} \tilde{u}_o}{2} - \tilde{u}_o + 2 \cos(\tilde{\gamma} \tilde{x} + \phi) \tilde{u}_o^* \tilde{w}_o &= 0 \\
i\partial_{\tilde{z}} \tilde{w}_o + \frac{\partial_{\tilde{x}\tilde{x}} \tilde{w}_o}{4} - \alpha \tilde{w}_o + 2 \cos(\tilde{\gamma} \tilde{x} + \phi) \tilde{u}_o^2 &= 0
\end{aligned} \tag{4.27}$$

The conserved quantities \tilde{Q} and \tilde{H} are defined similarly to (4.19) and (4.22), respectively; the relationship $Q = \beta\sqrt{\beta}\tilde{Q}$ holds.

z-invariant solutions satisfy the ODE system:

$$\begin{aligned}\frac{\tilde{u}''}{2} - \tilde{u} + 2\cos(\tilde{\gamma}\tilde{x} + \phi)\tilde{u}\tilde{w} &= 0 \\ \frac{\tilde{w}''}{4} - \alpha\tilde{w} + 2\cos(\tilde{\gamma}\tilde{x} + \phi)\tilde{u}^2 &= 0\end{aligned}\tag{4.28}$$

and can be taken real because all the involved parameters are real. Equivalently, the system (4.18) with no walk-off for SHG-hom reduces to (4.28) with $\gamma = 0$ [100]. Solitary solutions depend on position relative to the lattice, consequently on the lack of translational symmetry of eqs. (4.28) in \tilde{x} . Let us consider the solitary solution centered in $\tilde{x} = 0$ and allow the parameter ϕ , accounting for the position relative to the lattice, to vary in the interval $[0, \pi/2]$. ϕ can always be brought in this interval with a transformation involving just the sign of functions \tilde{u} and \tilde{w} . The parameter $\tilde{\gamma}$ refers to the transverse size of the soliton with respect to the lattice period. Let us focus on the case of bright one-hump FF solutions. Some preliminary considerations can be done in specific limits.

In the limit $\tilde{\gamma} \rightarrow 0$ the soliton width is small compared to the periodicity. The system can be considered as homogeneous with a perturbation of the nonlinear quadratic coefficient: the momentum is conserved and a particle-like approach can be adopted for a soliton falling in the classic family of non-walking simultons. It is known that this system allows bright solitary waves for $\alpha > 0$: a family of one-hump spatial solitons exists for every $\alpha > 0$ and classes of multi-hump unstable solitons can be found in the interval $\alpha = [0, 1]$. The one-hump solitary family has peculiar properties to be described in the context of the following analysis, the most important being the range of instability restricted to $\alpha < \alpha_c \approx 0.1$ [106]. For $\phi = 0$ and the beam is centered in the maximum of the nonlinearity, the first order perturbation to the homogeneous system is zero, and then the soliton can exist and be stable. For $\phi \neq 0$ the solitary wave experiences a gradient in nonlinearity; following Baronio *et al.* and Capobianco *et al.*, [107, 108] it can be stated that the soliton moves towards the maximum nonlinearity, then stable solitons are not expected in this approximation for $\phi \neq 0$. Note that, since the system is power normalized, it will always exist a power level large enough to make $\tilde{\gamma}$ small.

Kerr limit

Interesting results are obtained in the Kerr limit, when $\alpha \gg 1$. Eqs. (4.28) reduce to the usual NLS: [100]

$$\begin{aligned} \frac{\tilde{u}_o''}{2} - \tilde{u}_o + \frac{4}{\alpha} \cos(\tilde{\gamma}\tilde{x} + \phi)^2 \tilde{u}_o^3 &= 0 \\ \tilde{w}_o &= \frac{2}{\alpha} \cos(\tilde{\gamma}\tilde{x} + \phi) \tilde{u}_o^2 \end{aligned} \quad (4.29)$$

The nonlinear coefficient is periodic with $\tilde{\gamma}$ and the SH changes sign according to it. While a great effort has been devoted to investigating structures with both linear and nonlinear periodic refractive indices, [109], only a few studies have considered a periodicity exclusively in the nonlinear coefficient and none of them addressed physical structures in optics. [110, 111] Some theoretical results can be found in Refs. [111, 112] and adapted to this case.

The case with $\tilde{\gamma}$ small has also been previously addressed: solitary waves can always be found and are stable when centered in the maximum of the nonlinear refractive index ($\phi = 0$). Solitary waves centered in the minimum ($\phi = \pi/2$) can also be found, but are unstable as they tend to move towards regions with higher nonlinearity.

In the limit $\tilde{\gamma} \gg 1$, the soliton is wide compared to the period and the average nonlinearity plays an important role. Solitary solutions can be derived from the NLS using mean nonlinear properties, the periodicity intervening only as a second-order correction in $1/\tilde{\gamma}$. The solutions are stable.[112].

Families of solitary solutions for $\alpha > 0$

Eqs. (4.28) can be numerically solved for any α with a relaxation method. [53]

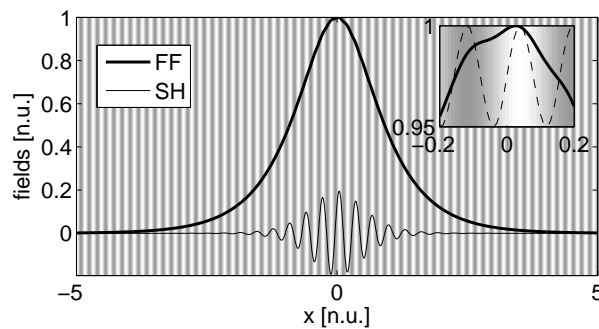
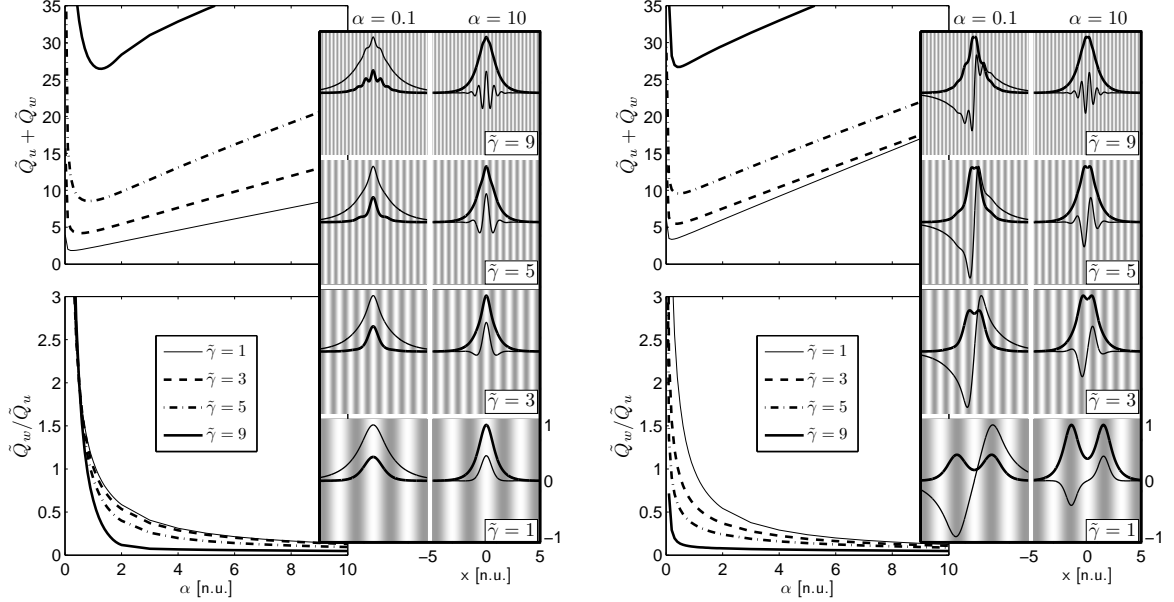


Figure 4.2: Asymmetric solitary solution in the Kerr limit for large periods. In this simulation $\tilde{\gamma} = 20$, $\alpha = 10$ and $\phi = \pi/4$. The thin line is the SH, which follows the grating periodicity as visible by the gray pattern reproducing the modulation of the quadratic nonlinearity $\cos(\tilde{\gamma}\tilde{x} + \phi)$. The thick line is the FF, a sech-type function with a small correction due to the periodicity, visible in the inset where the FF (thick line) is reported with the nonlinear refractive index $\cos(\tilde{\gamma}\tilde{x} + \phi)^2$ (dashed line).



(a) $\phi = 0$. Even solitary solutions for $\tilde{\gamma} = 1, 3, 5, 9$. Left: total energy (top) and ratio between SH and FF energies (bottom) versus mismatch α . Right, solitary profiles at low and high α (left and right columns), respectively.

(b) $\phi = \pi/2$. Odd solitary solutions for $\tilde{\gamma} = 1, 3, 5, 9$. Left: total energy (top) and ratio of SH to FF energies (bottom) versus α . Right, solitary profiles at low and high α (left and right columns), respectively.

Figure 4.3: Family of solitary solutions symmetric with respect to the origin

In the limit $\tilde{\gamma} \gg 1$ and $\alpha \gg 1$ sech-type solutions are found for the FF at any ϕ , while the SH exhibits the zeroes of the periodicity. As previously pointed out, even the FF possesses a small correction due to the grating. Fig. 4.2 shows an example with $\tilde{\gamma} = 20$ and $\alpha = 10$.

Far from the limit of large $\tilde{\gamma}$ and large α , solitary solutions exist for $\phi = 0$ and $\phi = \pi/2$. In these cases, since the structure possesses a symmetry with respect to the origin, it is convenient to look for odd and even solutions. The SH must follow the parity of the nonlinear periodicity, as the nonlinear term in the Hamiltonian $\int \cos(\tilde{\gamma}\tilde{x} + \phi) \tilde{u}^2 \tilde{w} d\tilde{x}$ has to be nonzero. If this term were null, the equivalent variational problem 4.24 would be linear and would not support solitary waves.

Two classes of solution adiabatically varying with α are found for every $\alpha > 0$ and even and odd grating symmetries. Fig 4.3 summarizes the properties of such solutions. For large $\tilde{\gamma}$ and large α both classes fall in the case of Fig. 4.2. As the mismatch parameter α decreases, the energy of the SH increases compared to the FF energy and the number of zeroes in the SH decreases. For small α the SH profile has one or two humps in even and odd cases, respectively, while the FF has no zeroes. For $\tilde{\gamma} \rightarrow 0$, even and odd classes fall back in the one-hump solitary waves of SHG-hom and in the null solution, respectively. Some general features of the simultons are preserved: energy and relative weight of the SH increase as the mismatch α decreases. Larger energies are

required to obtain solitary waves for larger $\tilde{\gamma}$ at given α , as the transverse grating makes the SH diffract more than in homogeneous media.

Stability

The stability can be discussed by studying the evolution of a small perturbation of the solitary solutions and solving the resulting linearized eigenvalue problem. This is a standard approach, [29, 105] introduced in 1973 by Vakhitov-Kolokolov [113] in a seminal work on the stability of Kerr-like solitons and used in 1981 by Kanahsov and Rubenichik in a pioneering paper on solitary waves in quadratic media. [114]; the same approach was later applied to stability of (type I, type II) SHG quadratic non-walking and walking solitons [106, 115–117]. Eqs. 4.27 are linearized by the substitutions: $\tilde{u} = \tilde{u}_o + \delta\tilde{u}e^{\lambda z}$, $\tilde{w} = \tilde{w}_o + 2\delta w e^{\lambda z}$ with $\delta u, \delta w$ small with respect to the solitary solutions \tilde{u}_o, \tilde{w}_o . Expressing the solutions in real and imaginary parts as $\delta u = u_R + iu_I$ and $\delta w = w_R + iw_I$, the eigenvalue system is obtained for $\mathbf{v} = \mathbf{v}_R + i\mathbf{v}_I$, with $\mathbf{v}_R = (u_R, w_R)$ and $\mathbf{v}_I = (u_I, w_I)$:

$$\begin{aligned}\mathcal{L}_+\mathbf{v}_R &= \lambda\mathcal{S}\mathbf{v}_I \\ \mathcal{L}_-\mathbf{v}_I &= -\lambda\mathcal{S}\mathbf{v}_R\end{aligned}\tag{4.30}$$

with null boundary conditions at $x \rightarrow \pm\infty$ for the functions and their derivatives, being $\mathcal{S} = \begin{pmatrix} 1 & 0 \\ 0 & 2 \end{pmatrix}$ and

$$\mathcal{L}_{\pm} = \begin{pmatrix} \frac{\partial_{\tilde{x}\tilde{x}}}{2} - 1 \pm 2w_o \cos(\tilde{\gamma}\tilde{x} + \phi) & 4u_o \cos(\tilde{\gamma}\tilde{x} + \phi) \\ 4u_o \cos(\tilde{\gamma}\tilde{x} + \phi) & \frac{\partial_{\tilde{x}\tilde{x}}}{2} - 2\alpha \end{pmatrix}\tag{4.31}$$

self-adjoint operators.

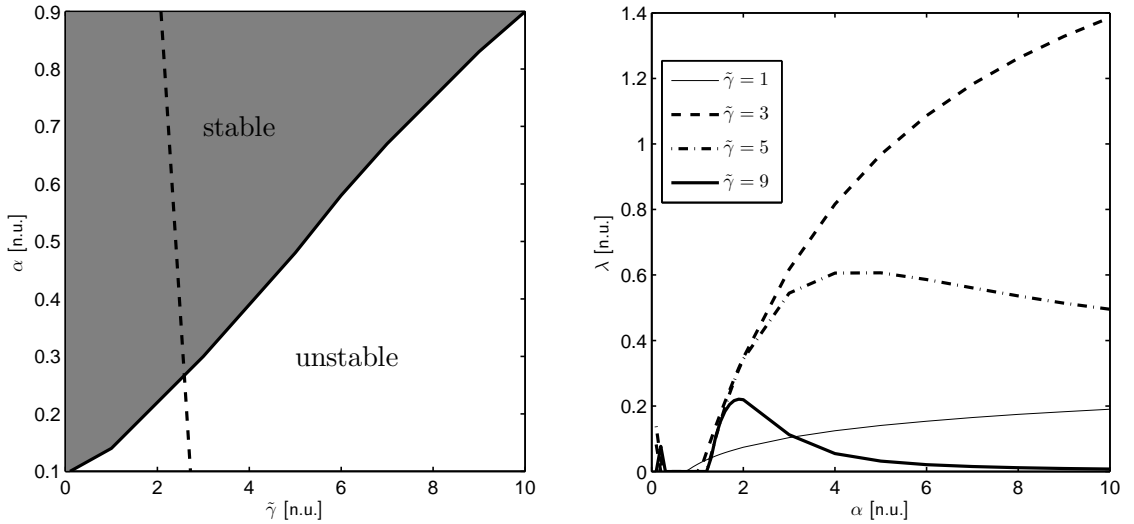
It is important to underline that system 4.30 can be obtained without assuming $\delta w/w_o \ll 1$ (and then $\delta w = 0$) at the zeroes of the SH, as they correspond to the zeroes of the nonlinearity and there the perturbation δw is completely general. Although the two operators are self-adjoint, the complete eigenvalue problem is not. Nonetheless, several general comments can be made. The kernel of the problem consists of a number of solutions equal to the number of symmetries of the original nonlinear problem (4.28); it possesses just one vector \mathbf{v}^K associated to the conservation of energy, with $\mathbf{v}_R^K = 0$ and $\mathbf{v}_I^K = (u_o, w_o)$, the latter solution to the problem $\mathcal{L}_-\mathbf{v}_I = 0$. The operator \mathcal{L}_+ has a void kernel, as the numerical analysis confirms. For $\tilde{\gamma} = 0$, due to translational symmetry, it has $(\partial_x u_o, \partial_x w_o/2)$ as kernel.

In significant cases \mathcal{L}_- is defined positive in the space orthogonal to its kernel \mathbf{v}_I^K . The numerical analysis shows that this happens for the class of even solutions previously

presented for $\phi = 0$: when both u_o and w_o have no zeroes (small α), this occurrence is rigorously stated by the oscillation theorem. [118]

When \mathcal{L}_- is positive, it is invertible and its inverse is positive; then system (4.30) can be rewritten as the generalized eigenvalue problem $\mathcal{L}_+ \mathbf{v}_R = -\lambda^2 \mathcal{S} \mathcal{L}_-^{-1} \mathcal{S} \mathbf{v}_R$ with eigenvalue λ^2 always real. As a consequence, system (4.30) possesses purely imaginary or real eigenvalues λ , the latter defining unstable solutions. The stability threshold is defined by the eigenvalue $\lambda = 0$ at $\alpha = \alpha_c$ and $\tilde{\gamma} = \tilde{\gamma}_c$; the corresponding eigenvector belongs to the kernel of system (4.30), i. e. it is proportional to \mathbf{v}^K (in the case $\tilde{\gamma} = 0$ it can be demonstrated that the eigenvector corresponding to $\alpha = \alpha_c$ is always orthogonal to $\mathbf{v}_R = (\partial_x u_o, \partial_x w_o/2)$ and $\mathbf{v}_I = 0$). [106] The solvability condition for a slightly unstable solution (i.e. for small λ) provides a criterion for the instability threshold. [106] Close to threshold, the unstable eigenvector can be expanded in series of λ as $\mathbf{v} = \mathbf{v}^{(0)} + \lambda \mathbf{v}^{(1)} + \lambda^2 \mathbf{v}^{(2)} + o(\lambda^3)$. The solution at the zero-th order is $\mathbf{v}^{(0)} = \mathbf{v}^K$. At the first order the equation $\mathcal{L}_+ \mathbf{v}_R^{(1)} = \mathcal{S} \mathbf{v}_I^K$ holds valid. An analytical solution for this correction is:

$$\begin{aligned} u_R^{(1)} &= u_o + (2 - \alpha) \partial_\alpha u_o + \frac{x}{2} \partial_x u_o - \tilde{\gamma} \partial_{\tilde{\gamma}} u_o \\ w_R^{(1)} &= \frac{1}{2} (w_o + (2 - \alpha) \partial_\alpha w_o + \frac{x}{2} \partial_x w_o - \tilde{\gamma} \partial_{\tilde{\gamma}} w_o) \end{aligned} \quad (4.32)$$



(a) Range of stability for even solitary waves with $\phi = 0$. The dashed line indicates the condition of phase matching $\Delta_o = 0$.

(b) Instability gain for odd solitary waves with $\phi = \pi/2$ and $\tilde{\gamma} 1, 3, 5, 9$. For large $\tilde{\gamma}$ and large α the instability gain approaches zero.

Figure 4.4: Simulton stability

At next order the equation is $\mathcal{L}_-\mathbf{v}_I^{(2)} = -\mathcal{S}\mathbf{v}_R^{(1)}$. Owing to the Fredholm alternative, the solution of this problem requires the orthogonality between $\mathcal{S}\mathbf{v}_R$ and \mathbf{v}_K and the following condition holds:

$$\int u_o u_R^{(1)} + 2w_o w_R^{(1)} dx = 0 \rightarrow \quad (4.33)$$

$$\frac{3}{4}\tilde{Q} + \frac{(2-\alpha)}{2}\partial_\alpha\tilde{Q} - \frac{\tilde{\gamma}}{4}\partial_{\tilde{\gamma}}\tilde{Q} = \frac{1}{2\sqrt{\beta}}\partial_\beta Q = 0 \quad (4.34)$$

The latter equality considers the energy Q defined in physical units, and can be easily checked by a direct expansion. Remarkably, the relation (4.34) requires $\partial_\beta Q = 0$, which is the VK criterion applied to a wide class of solitary waves. The stability domain obtained from this relation and numerically checked by direct integration of system (4.30) is shown in Fig. 4.4(a). While decreasing with $\tilde{\gamma}$, the stability region remains remarkably large for any $\tilde{\gamma}$.

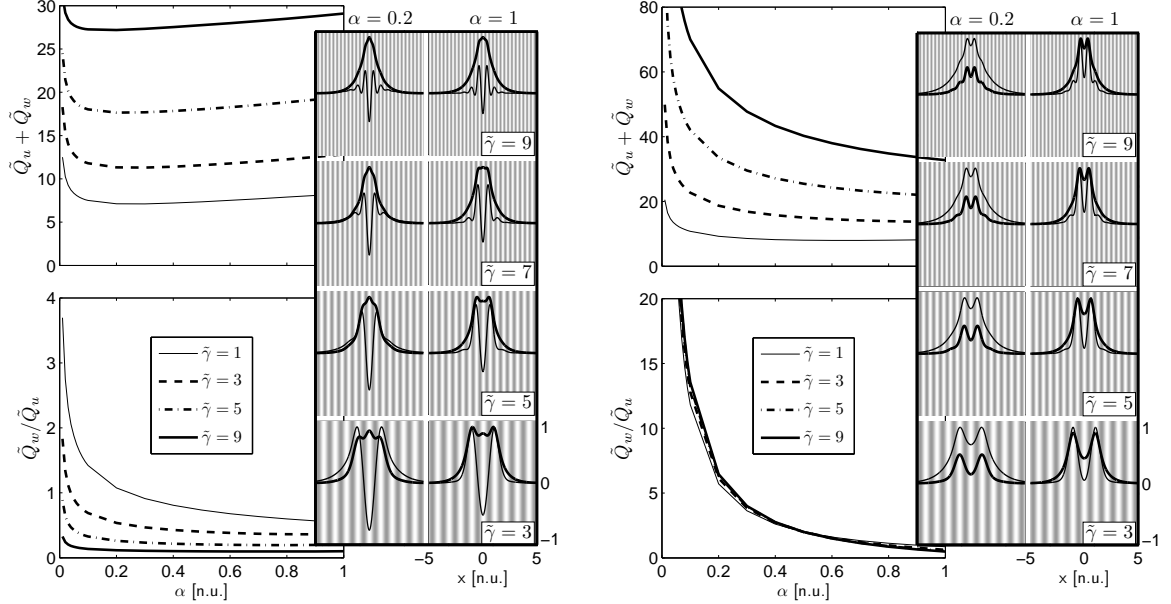
For odd solutions when $\phi = \frac{\pi}{2}$, the operator \mathcal{L}_- is not defined positive and, then, only direct numerical integrations of system (4.30) are possible. A positive eigenvalue λ exists for every $\tilde{\gamma}$ in a wide α range and the solutions are mostly unstable. The numerically evaluated maximum eigenvalues are graphed in Fig. 4.4(b). The rate of instability λ decreases asymptotically, converging to a stable condition for growing $\tilde{\gamma}$ and α .

The linearized system $\mathcal{L}_-\mathbf{v}_I^K = 0$, solved by $\mathbf{v}_I^K = (u_o, w_o)$, gives information on the existence range of bright solitary waves. For $x \rightarrow \pm\infty$ u_o and $w_o \rightarrow 0$, the solution \mathbf{v}_I^K tends towards $(e^{\mp\Omega_u \tilde{x}}, e^{\mp\Omega_w \tilde{x}})$, with $\Omega_u = \sqrt{2}$ and $\Omega_w = 2\sqrt{\alpha}$. In the case of the FF, the solution always decays, correctly describing the behavior of the function u_o . Conversely, for the SH when $\alpha < 0$, a decay does not occur: the solution w_o must oscillate at infinity, in contrast to the hypothesis of a bright soliton. $\alpha < 0$ is therefore the non-existence condition of *all* bright solitary waves, as in the SHG-hom case.

Other classes of solutions

Before concluding this section, a few comments need be made on other classes of solution found by numerical integration of system (4.28), for both even and odd perturbations. It is known that, for simultons of a homogeneous nonlinearity, other multi-hump solitary solutions can be found for α in $[0, 1]$ and are unstable. In the same range and in the presence of the grating, some classes of unstable solutions can be found but, due to the periodicity, they are hardly classified as one-hump or multi-hump; two examples are shown in Fig. 4.5.

Concluding this section, several families of solitary bright solutions are found for $\vartheta = 0$. The class of even solitary solutions centered in the maximum of the nonlinearity is the most interesting for its extended range of stability. This class exists for every



(a) $\phi = 0$. Solitary solutions for $\tilde{\gamma} = 1, 3, 5, 9$. Left: total energy (top) and ratio of SH to FF energies bottom) versus mismatch α . Right: solitary profiles at low and high α (left and right columns), respectively.

(b) $\phi = 0$. Solitary solutions for $\tilde{\gamma} = 1, 3, 5, 9$. Left: total energy (top) and ratio of SH to FF energies bottom) versus mismatch α . Right: solitary profiles at low and high α (left and right columns), respectively.

Figure 4.5: Two families of solitary solutions symmetric with respect to the origin for $\alpha < 1$

$\alpha > 0$ which, in physical terms, defines the nonlinear phase cut-off for soliton formation $\beta_{cut} = \max(0, \frac{1}{2}[(\frac{\gamma}{2})^2 - \Delta_o])$. This β_{cut} is the same for walking solitons propagating along the FF, when the SH exhibits a walk-off angle of $|\gamma/2|$, [115, 117, 119] the modulus of the walk-off angles of the two plane waves in which the SH can be formally decomposed in the linear regime, as described in section 4.1.1.

4.2.2 Asymmetric case

In the case of $\vartheta \neq 0$ eqs. (4.23) hold. The previously studied solutions can be readily transposed to this system, noting that eqs. (4.23) admit solutions of the form $u_o = u_m(x)e^{i\vartheta x}$ and $w_o = w_m(x)e^{2i\vartheta x}$, with u_m and w_m real. With this assumption and the previous transformation with $\vartheta = \sqrt{\beta}\tilde{\vartheta}$, the system can be recast as:

$$\begin{aligned} \frac{\tilde{u}_o''}{2} - (1 - \frac{\tilde{\vartheta}^2}{2})\tilde{u}_o + 2\cos(\tilde{\gamma}\tilde{x} + \phi)\tilde{u}_o\tilde{w}_o &= 0 \\ \frac{\tilde{w}_o''}{4} - (\alpha - \tilde{\vartheta}^2)\tilde{w}_o + 2\cos(\tilde{\gamma}\tilde{x} + \phi)\tilde{u}_o^2 &= 0 \end{aligned} \quad (4.35)$$

Evidently it shares the properties (and solutions) of eqs. (4.28) after a suitable normalization. It is worth commenting briefly on the existence of solitary waves of eqs. (4.35). Following the previous approach, two conditions define the domain of non-existence for bright solitary waves: $\tilde{\vartheta} < \sqrt{2}$ and $\alpha > \tilde{\vartheta}^2$. [115, 119] In physical coordinates, the relations become $\beta_{cut} = \frac{1}{2} \max(\vartheta^2, (\frac{\gamma}{2})^2 + \vartheta^2 - \Delta_o)$ which, even in this case, is the cut-off threshold of a soliton walking at an angle ϑ with respect to the FF, with an SH propagating with a walk-off of modulus $\gamma/2$ with respect to the fundamental. [115, 119]

Large θ case

A physically relevant situation is obtained when the angle θ is large enough to markedly separate in wavelength the two PM conditions associated with the two reciprocal vectors G_{10} and G_{01} . It is then convenient to go back to eqs. (4.17) using physical quantities. Specifically, when $\Delta_o \mp \gamma\vartheta \approx 0$ and $\gamma\vartheta \gg 1$ (i.e. in PM for $G_{10}(G_{01})$ and in cascading for $G_{01}(G_{10})$), respectively), performing a multiscale expansion as in Conti *et al.*[120] and with the substitution $w = w'e^{\pm i\gamma x}$, eqs. (4.17) can be recast in the following form, where the out of resonance condition $\Delta_o \pm \gamma\vartheta$ plays the role a cubic role via cascading (of different signs in the two cases):

$$\begin{aligned} i\partial_z u + \frac{\partial_{xx} u}{2} + u^* w' + \frac{1}{\Delta_o \pm \gamma\vartheta} (|u|^2 - |w'|^2) u &= 0 \\ i\partial_z w' + \frac{\partial_{xx} w'}{4} \pm i\frac{\gamma}{2} \partial_x w' - (\Delta_o \mp \gamma\vartheta) w' + u^2 - \frac{2}{\Delta_o \pm \gamma\vartheta} |u|^2 w' &= 0 \end{aligned} \quad (4.36)$$

Here u and w represent the zero order approximation to the original function for an expansion in $1/(\Delta_o \pm \gamma\vartheta)$. System (4.36) is translationally invariant in x and z ; it also conserves Hamiltonian and momentum. The equations are reduced to a classical problem of competing nonlinearities, largely addressed in literature [100], where the quadratically induced Kerr effect is asymmetric versus FF and SH [120, 121], being equivalent to XPM for both waves and SPM for the FF (with different sign). System (4.36) falls among the standard equations for quadratic walking solitary waves [119] when $\gamma\vartheta$ is large enough to completely neglect the resonant interaction. The Kerr-like cascaded term is peculiar of QPM structures, because the nonlinear periodicity always provides high order momenta far from PM and in the cascading approximation. [122] In this case, the Kerr effect is generated by a momentum of the same order of magnitude of the resonant vector and can be generally stronger than in standard 1D QPM gratings. [122] It is interesting to note, when taking into account these terms, the asymmetry of the structure for $\theta \neq 0$ is included in the description as the Kerr ruling term $\Delta_o \pm \gamma\vartheta \approx \pm\gamma\vartheta$ is of opposite signs for the two resonances. Therefore, even if eqs. (4.17) admit transverse invariant solutions when propagating in the ϑ direction, it is possible to find an approximated system which admits standard walking solitary waves.

It is important to stress that eqs. (4.17) *are not equivalent* to the following eqs. (4.37) obtained by superimposing two SH waves satisfying PM conditions at the two angles, with $w = w_{10}e^{i\gamma x} + w_{01}e^{-i\gamma x}$:

$$\begin{aligned} i\partial_z u + \frac{\partial_{xx} u}{2} + u^*(w_{10} + w_{01}) &= 0 \\ i\partial_z r + \frac{\partial_{xx} w_{10}}{4} + i\frac{\gamma}{2}\partial_x w_{10} - (\Delta_o - \gamma\vartheta)w_{10} + u^2 &= 0 \\ i\partial_z w_{01} + \frac{\partial_{xx} w_{01}}{4} - i\frac{\gamma}{2}\partial_x w_{01} - (\Delta_o + \gamma\vartheta)w_{01} + u^2 &= 0 \end{aligned} \quad (4.37)$$

Eqs. (4.37) lead to similar approximation of eqs. 4.17 in the no-depletion regime and when at least one of the nonlinear resonances is in the cascading regime (e.g. in the case of eqs. (4.36)). Eqs. (4.37) require the conservation of $Q' = \int |u|^2 dX + \int |w_{10}|^2 dX + \int |w_{01}|^2 dX$ which is *not* the energy of the system, apart from some specific cases as previously mentioned. Hamiltonian and momentum are conserved also. Eqs. (4.37) lead to walking solitary solutions in every regime but, since the phases of FF and SH's are *locked* in this condition, the quantity Q' has no physical meaning unless one of the two SH's w_{10} and w_{01} is negligible, i.e. in the cascading limit for one of the resonances.

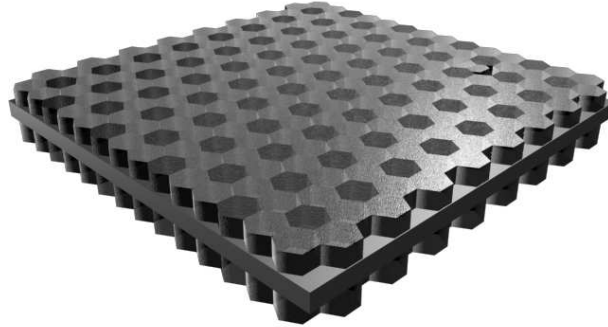


Figure 4.6: Sketch of a HexLN planar waveguide.

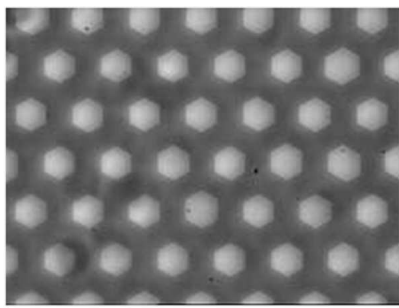
4.3 Experiments on simultons in a 2D nonlinear lattice: HexLN

4.3.1 HexLN planar waveguide and experimental setup

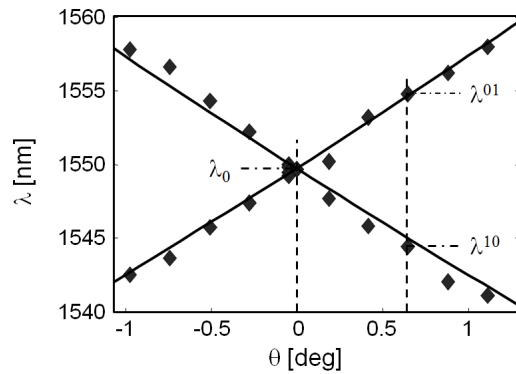
The sample used for the experiments described in the next paragraphs is an Hexagonally poled Lithium Niobate (HexLN) waveguide fabricated at the *Optoelectronic Research Centre*, University of Southampton.

Fig. 4.6 is a 3D sketch of an actual HexLN planar waveguide. The 2D QPM structure was obtained in a $500\text{ }\mu\text{m}$ -thick congruent z-cut LN crystal, using electric field poling via liquid electrodes and a photoresist mask with a hexagonal pattern (8 mm wide and 18 mm long) of period $\Lambda = 16.4\text{ }\mu\text{m}$. The planar waveguide was fabricated by the sequence of PE in benzoic acid for 29 h at 170°C , thermal annealing at 200°C for 13 h and at 330°C for 7 h. Finally the slab was reverse proton exchanged (RPE) in an eutectic melt of LiNO_3 , NaNO_3 and KNO_3 at 320°C for 28 h. These steps resulted in a buried planar waveguide $2.9\text{ }\mu\text{m}$ beneath the crystal surface, supporting only one mode (TM_0) at the pump wavelengths in the C-band for optical communications. In such a structure the Fourier coefficient $d_{10} = d_{01} = d_o = \frac{3}{\pi^2}$

Measurements in the no-depletion regime were performed by Gallo *et al.* [123] The resulting SHG resonant wavelengths λ_{10} and λ_{01} versus FF incidence angle θ are graphed in Fig. 4.7(b). From the relation (4.13) and, since for small values Δk_o is linear with wavelength, a linear trend exists for λ versus θ , with:



(a) Micrograph of an HexLN sample



(b) SHG resonant wavelengths (λ) versus FF incidence angle (θ): measurements (diamonds) and linear fits (solid lines). [123]

Figure 4.7: HexLn Sample

$$\Delta k^{10/01}|_{cm^{-1}} = -1.54\pi(\lambda_{FF} - \lambda_0)|_{nm} \mp 12.3\pi\theta|_{deg}. \quad (4.38)$$

For $\theta > 0$, if $\lambda = \lambda_{01}$ then $\Delta k^{10} < 0$; if $\lambda = \lambda_{10}$ then $\Delta k^{01} < 0$. By defining $\lambda^- = \lambda_{01}$ and $\lambda^+ = \lambda_{10}$, it is easy to keep in mind the sign of the out of resonance mismatch for $\theta > 0$. For the experiments, the HexLN waveguide was mounted on a piezo-electrically controlled stage, temperature stabilized at $\sim 85^\circ\text{C}$ to prevent photorefractive damage. The setup (Fig.0.1) is similar to the one described in the previous chapter. The main differences are the presence of a goniometer (to adjust the FF angle of incidence) and of a cylindrical lens to shape the FF beam into a cylindrical Gaussian spot, end-fire coupled to launch the TM_0 waveguide mode. The FF beam had lateral and vertical waists of $27.5 \mu\text{m}$ and $3.4 \mu\text{m}$, respectively and its propagation in the 18 mm-long sample amounted to ~ 5.4 Rayleigh lengths. At the sample output, FF and SH were monitored by time-gated photodiodes and imaged with either 10x or 5x microscope objectives onto a Vidicon camera or a CCD, respectively. The images were filtered to reduce background noise.

4.3.2 Observation of Quadratic Spatial Solitons in a HexLN waveguide

The angular position of the sample with respect to the input beam was verified by performing an SHG efficiency measurement versus detuning (i.e. wavelength) as, as described for SPP-LN channel waveguides in chapter 4. Fig. 4.8 shows two examples of SHG efficiency data versus FF wavelength in the no depletion regime, for symmetric and asymmetric excitation cases, respectively. The small oscillations in wavelength are due to a Fabry-Perot interference in the beam-splitter used to spill a portion of the input power. Due to the finite width of the resonance curve, the angle of the sample could be

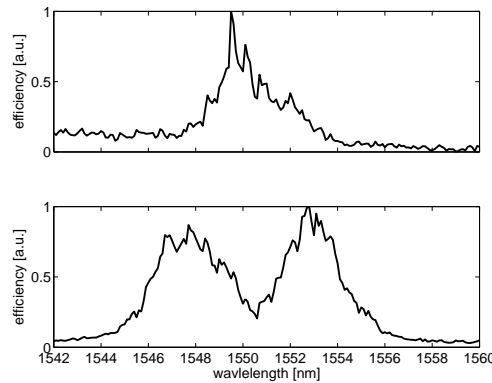


Figure 4.8: SHG efficiency in the nodepletion regime for the symmetric ($\theta < 0.1^\circ$, top) and asymmetric cases ($\theta \approx 0.5^\circ$, bottom), respectively.

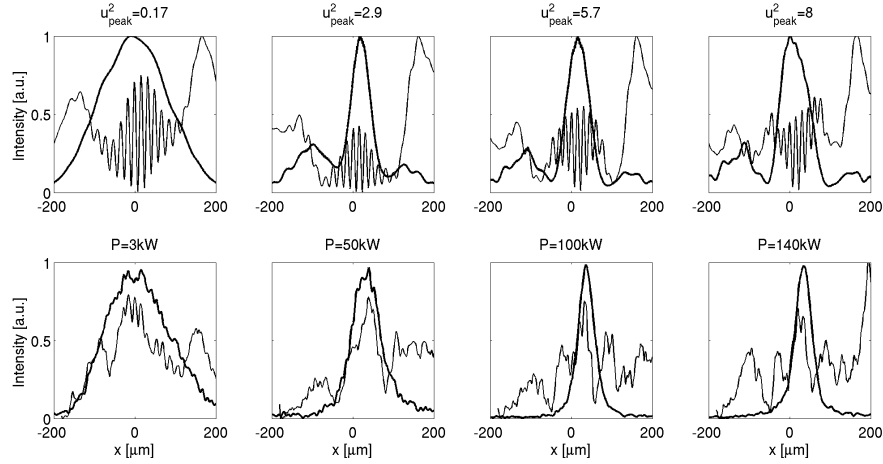
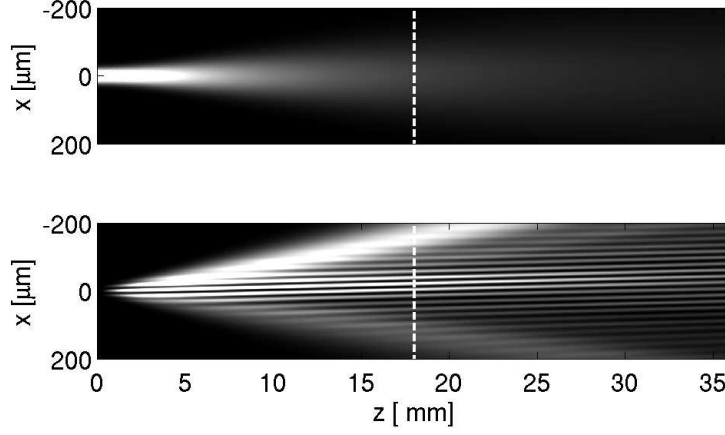


Figure 4.9: Nearly symmetric case. Top: simulated output profiles obtained from eqs. (4.17) with an input Gaussian FF beam and $\gamma = 6.1$, $\theta = 0.05^\circ$, $\lambda = \lambda^+ + 1.5nm$ with peak u_{peak}^2 equal 0.2, 2.9, 5.7 and 8, respectively. The abscissa is x expressed in measurable units. Bottom: acquired output profiles for input powers of 3, 50, 100, and 140 kW, respectively, at $\lambda = 1551nm$

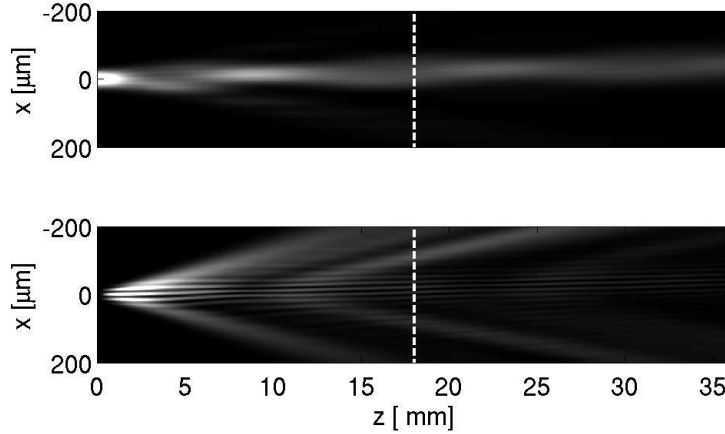
determined with a lower accuracy in the symmetric case than in the asymmetric case. From relation (4.38), an error of $2nm$ on the peak wavelength corresponds to about 0.1° on the angle. Eqs. (4.17) was used for the numerical fit of the experimental data. The size of the beam with respect to the QPM period determined $\gamma \approx 6$ normalized units in system (4.17). In the following, it is convenient to express the simulation parameters ϑ and Δ in the observable angle θ and wavelength λ , easily linked to mismatch using (4.38).

Symmetric Case

In this case, spatial solitons as described in the paragraph 4.2.1 are expected. The first experimental measurements were carried out at a wavelength of $1551nm$, approximately $1.5nm$ above the resonance shown in Fig. 4.8 (top) in order to obtain a small positive mismatch Δk . The simulated and measured output intensity profiles for the FF (thick line) and the SH (thin line) are displayed in fig. 4.10. The actual images were collected using a Vidicon camera. the simulations were performed using a BPM method similar to the one described in the previous chapters, assuming the experimental quantities and an FF angle of incidence $\theta = 0.07^\circ$. At low power the FF beam diffracted. As foreseen, the SH resembled two beams propagating with opposite angles with respect to the FF excitation: two lateral wings and interference fringes in the center are apparent in the intensity profiles, despite the blooming effect of the camera. The calculated beam propagation in the no-depletion regime is shown in Fig. 4.10(a), with white dashed lines indicating the output section of the actual sample.



(a) Calculated FF (top) and SH (bottom) intensity evolution of an input FF Gaussian beam with peak $u_{peak}^2 = 0.2$: diffractive regime.



(b) Calculated FF (top) and SH (bottom) intensity evolution 4.17 for an input FF Gaussian beam with peak $u_{peak}^2 = 8$. Quasi solitary regime.

Figure 4.10: Nearly symmetric case. Calculated intensity evolution from eqs. (4.17) for $\gamma = 6.1$, $\theta = 0.05^\circ$, $\lambda = \lambda^+ + 1.5nm$. The coordinates are x and z , in measurable units for convenience. The white dashed lines indicate the output of the actual sample.

At higher powers the FF reduced its waist and a small lateral shift occurred. The SH dynamics was more complex: the central part of the beam, where interference fringes were still visible, remained confined in a region of the same size of the FF. The number of lateral wings increased; this was visible at powers $> 100kW$ and indicated that FF and SH were exchanging energy in propagation. Firstly, the FF generated the SH; part of the SH diffracted in two *external* lateral wings but, when the SH intensity overlapping the FF was high enough, the energy flow was reversed and the SH downconverted in FF. Then the FF upconverted again and the two *internal* lateral wings were generated. This is visible in the simulations of Fig. 4.10(b), where it is apparent that when the

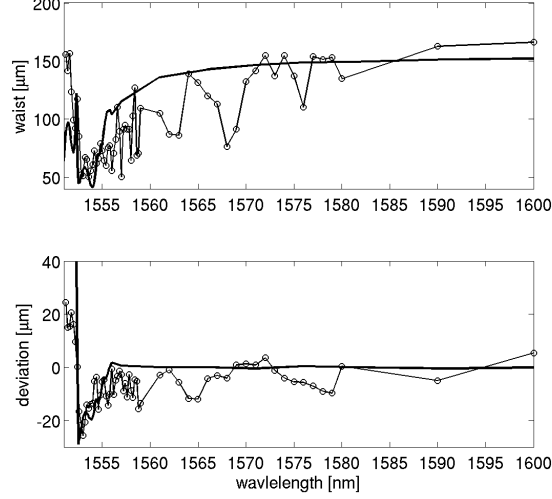
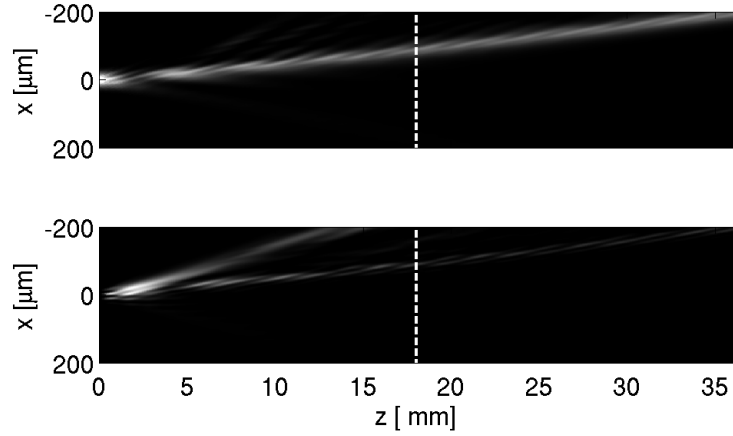


Figure 4.11: Nearly symmetric case with $P_{FF} = 25$ kW. Void circles: Evolution (top) of the FF output beam FWHM waist and (bottom) of the lateral displacement versus pump wavelength. Oscillations in waist are due to interference due to the two surfaces of the beam splitter BS. The solid line is a fit obtained 4.17 for $\gamma = 6.1$, $\theta = 0.07^\circ$ and $u_{peak}^2 = 2.2$

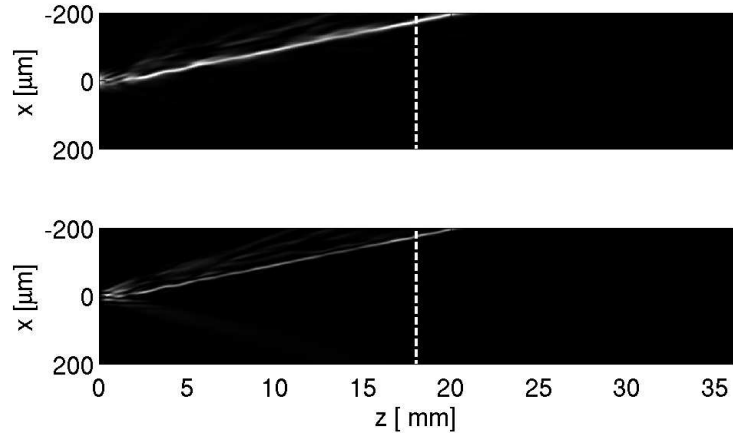
FF increases its energy no lateral generation occurs in the SH. Eventually FF and SH approach the simulton solution, in which no power exchange occurs between the two waves, beside energy sheds into radiation modes. In the simulations with $u_{peak}^2 = 8$ (corresponding to $140kW$), it can be appreciated that the central part of the coupled FF-SH intensity is nearly constant in propagation, and it progressively decreases the propagation losses. The excited solitary wave contains almost 60% of the input power and the ratio between the energies of SH and FF is close to 15%. The measured output strongly overlapped with the calculated solitary solution. The dimension of the FF waist at the output was approximately $44\mu m$ for powers of $100kW$ and $140kW$, indicating that the beam approached a solitary solution of larger size than the input beam. It is worth noticing that the beam was laterally shifted, following the orientation of the sample, as described in the first part of paragraph (4.2.2); the lateral shift was about $20\mu m$ for powers $> 100kW$ and a sample at an angle $\theta = 0.05^\circ$. The latter is the value used in the simulations, in remarkable agreement with the acquired profiles. Note that in such conditions eqs. (4.37) would not conserve the total power and the two SH waves would not interfere in the solitary regime.

The variation of the FF output waist (FWHM) at a fixed input power of $25kW$ is shown in Fig. 4.11 versus wavelength: self-focusing occurs for positive mismatches close to resonance. The lateral beam displacement measured as a mean value of the intensity distribution is also plotted. The simulations were performed with the previous parameters and for $u_{peak}^2 = 4$, in line with the experiments but higher than the previous set owing to the better coupling of light into the sample. Notice that the lateral dis-

placement is positive (opposite to the angle of orientation θ) for negative mismatches approaching the threshold.

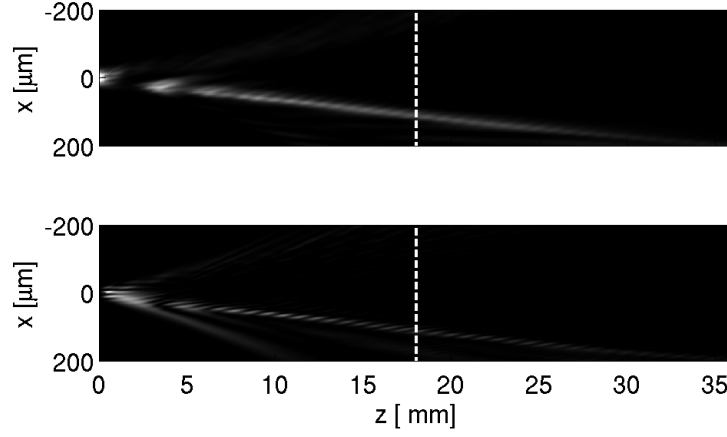


(a) Simulated FF (top) and SH (bottom) intensity evolution for a Gaussian input FF beam with peak $u_{peak}^2 = 25$, quasi solitary propagation: the soliton is shifted towards the direction of propagation of the SH in the no-depletion regime. Interference fringes are visible on the SH due to non collinear beam propagation due to the angle θ of sample orientation.

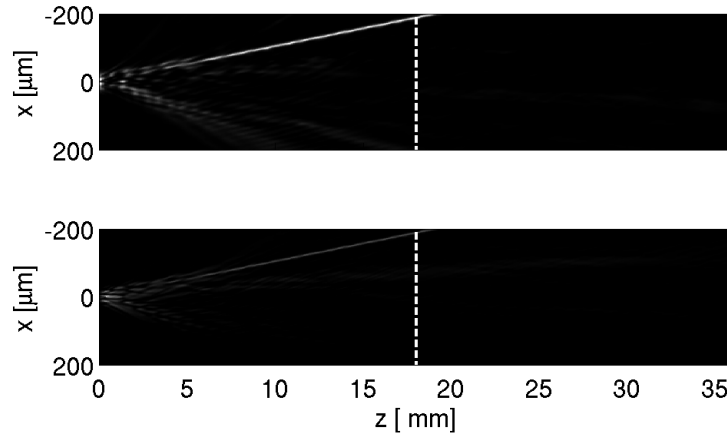


(b) Simulated FF (top) and SH (bottom) intensity evolution for a Gaussian input FF beam with peak $u_{peak}^2 = 144$, quasi solitary propagation: the soliton propagates at the angle θ of sample orientation. No interference fringes are visible at the SH.

Figure 4.12: Asymmetric case. Simulated intensity evolution obtained with eqs. (4.17) for $\gamma = 6.1$, $\theta = 0.6^\circ$, $\lambda = \lambda^+ + 1\text{nm}$. The coordinates are x and z , in measurable units for convenience. The white dashed lines indicate the output section of the actual sample.



(a) Simulated FF (top) and SH (bottom) intensity evolution for a Gaussian input FF beam with peak $u_{peak}^2 = 100$, quasi solitary propagation: the simulton is shifted towards the SH direction of propagation in the no-depletion regime. Interference fringes are visible at SH due to non collinear propagation in the sample at angle θ of orientation.



(b) simulated FF (top) and SH (bottom) intensity evolution for a Gaussian input FF beam with peak $u_{peak}^2 = 780$, quasi solitary propagation: the simulton propagates at the angle θ of orientation of the sample. No interference fringes are visible at SH.

Figure 4.13: Asymmetric case. Simulated intensity evolution from eqs. (4.17) for $\gamma = 6.1$, $\theta = 0.6^\circ$, $\lambda = \lambda^- + 1.nm$. The coordinates are x and z , in measurable units. The white dashed lines indicate the output section of the actual sample.

Asymmetric Case

In paragraph 4.2.2 two different scenarios were addressed in the asymmetric case. Strictly speaking solitons can be excited only along the direction of propagation θ , following the symmetry of the sample, and the solutions are of the same kind of those previously observed. Nonetheless, for large angles and for $\lambda = \lambda^+(\lambda^-)$ the system can be recast in

an approximated form that supports walking solitons, with one of the resonance in PM and the other in the cascaded limit. When excited by SHG, walking solitons propagate at an intermediate direction between the FF and the SH; hence, simultons propagating with positive and negative angles with respect to the FF can be expected for λ^+ and λ^- , respectively. In these two cases the contribution of the term out of resonance has opposite signs: for λ^+ the mismatch is positive and the cascaded term acts as a positive Kerr effect on the fundamental frequency, helping so lton formation when excited by SHG; for λ^- the mismatch is negative. Otherwise stated, when excited at λ^+ the solitary wave moves towards θ where the only profile-invariant solution exists, while in the other case the beam moves to the opposite direction. This intrinsic asymmetry of the resonant condition is explored numerically in figs. 4.12 and 4.13, for an angle $\theta = 0.6^\circ$, as used in the next set of experiments. At $\lambda \approx \lambda^+$ with $u_{peak}^2 = 25$ a nearly undiffracting beam propagates along the direction of the SH in the undepleted regime. The envelope is not constant in propagation, as the walking solitary solution results from a first order approximation of the system. This also occurs for a higher excitation $u_{peak}^2 = 100$ at $\lambda \approx \lambda^-$. Increasing the excitation for λ^+ , the self-confined beam moves till the solitary solution is formed at the angle θ with $u_{peak}^2 = 144$. In the λ^- case, the quasi invariance vanishes. At an excitation $u_{peak}^2 = 780$, a solitary solution in the only available direction is excited also in this case.

The experimental study of the asymmetric case must be conducted carefully. To obtain a symmetric shift of the FF beam at the two resonant wavelengths, a large angle θ is required. Taking into account the overall efficiency, an angle of propagation of

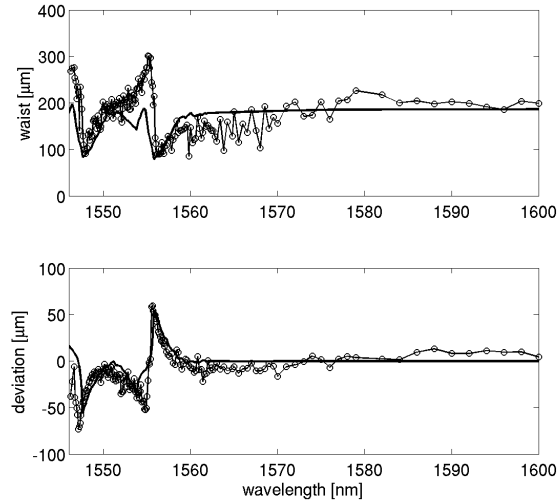


Figure 4.14: Asymmetric case with $P_{FF} = 22$ kW and $\theta = 0.6^\circ$. Symbols: (top) FF output waist (FWHM) and (bottom) lateral displacement versus input wavelength. Oscillations in waist are due to interference from the surfaces of the beam splitter. The solid line is a fit from eqs. (4.17) for $\gamma = 6.1$, $\theta = 0.6^\circ$ and $u_{peak}^2 = 1.4$

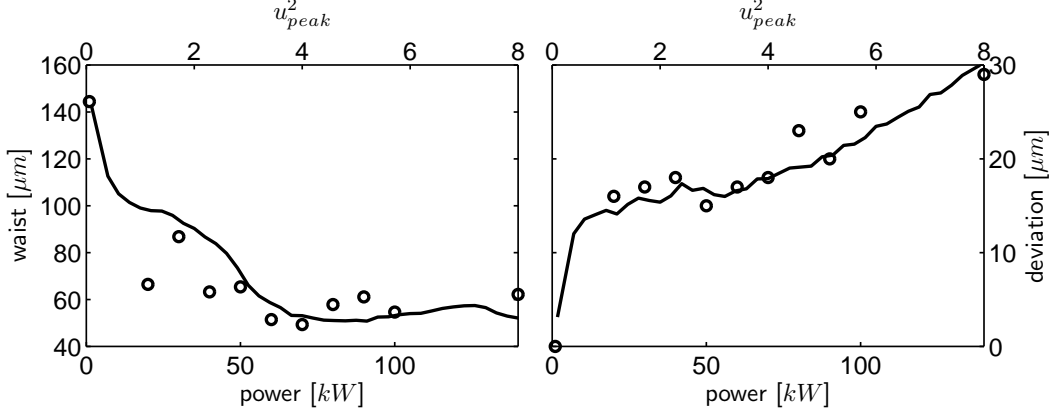


Figure 4.15: Asymmetric case. Experimental results for FF beam self-focusing at 1556nm at $\theta \approx 0.5^\circ$. Simulations were performed from eqs. (4.17) with a Gaussian FF input and $\gamma = 6.1$, $\theta = 0.5^\circ$, $\lambda = \lambda^+ + 2nm$. Circles: (left) FF output beam waist (FWHM) and (right) lateral displacement versus input power (bottom abscissa). The solid line is calculated versus u_{peak}^2 (top abscissa).

0.6° was adopted. For a peak power of $22kW$ self-focusing and shift of the FF beam were observed, as visible in Fig. 4.14. The simulations with $u_{peak}^2 = 1.4$ are in good agreement with the experimental results. The structure operates as at a wavelength controlled de-multiplexer with a self-confined output.

The beam self-confinement was investigated varying the input power at a fixed wavelength of 1556nm, close to λ^+ . Self-confinement and lateral shift in the quasi solitary regime was demonstrated, as visible in Fig. 4.15. Similar considerations apply to the SH.

For wavelengths close to λ^- a similar trend was never observed. This can be ascribed to the small deviation in the FF propagating angle due to the rotation of the half-wave plate used to control the input power. The deviation translates in a variation of the resonance. Self-confined beams with positive angles of propagation could be excited at almost every wavelength $> \lambda^+$; completely different is the situation for deviations to negative angles, with solitary propagation occurring only for a small range for wavelengths $> \lambda^-$.

4.4 Conclusions

This Chapter presented the first results on quadratic spatial solitons in a two-dimensional purely nonlinear lattice. The general equations were derived for two non-collinear concurrent QPM processes defined by two lattice vectors G_{10} and G_{01} , specifically addressing the analysis of a hexagonal geometry. Solitary propagation was investigated with the aid of the general equations, using Lie symmetry to demonstrate that solitary propagation can rigorously occur only along the bisector between the two lattice vectors. The numerical study of solitary propagation in these transversely periodic quadratic media yielded the existence of a class of simultons with a large stability domain, as analytically defined by the standard VK criterion. In this regime the structure behaves as a quadratically nonlinear waveguide. Extending known results on $\chi^{(2)}$ cascading, a regime could be identified where the general equations support walking solitary propagation, leading to the existence of two spectral regions for beam self-confinement and opposite displacements, where the structure operates as a wavelength controlled nonlinear de-multiplexer. The experimental demonstrations of self-confined propagation in the two regimes were summarized and interpreted. These results disclose a new richer scenario in the area of quadratic solitons as compared to solitons in uniform and 1D QPM quadratic media.

Chapter 5

Conclusions

In conclusion, in this dissertation I investigated, theoretically and experimentally, the propagation of picosecond light pulses in several materials of interest in nonlinear photonics. I studied the permanent effects of high energy pulses in colloidal opals doped with gold nanoparticles, resulting in a blue shift of the optical band gap; I examined spatial solitons, filamentation and conical emission in the ps regime in a novel heavy metal oxide glass, clarifying the role of nonlinear absorption in preventing catastrophic collapse; I performed second-harmonic generation using proton-exchanged channel waveguides in surface periodically poled lithium niobate and tantalate, modeling the effect of a limited depth in the induced nonlinear grating; I contributed to demonstrating quadratic multi-color spatial solitons in a nonlinear photonic lattice, finding new classes of simultons in a degenerate multiple quasi phase matching geometry.

In this PhD work new technologies and new materials were successfully employed in various nonlinear optics phenomena. The experimental results, after comparison with theoretical-numerical models and data analysis, have provided a quantitative evaluation of important physical features.

Bibliography

- [1] T. H. Maiman, “Stimulated optical radiation in ruby,” *Nature*, vol. 187, p. 493, 1960.
- [2] R. Y. Chiao, E. Garmire, and C. H. Townes, “Self-trapping of optical beams,” *Phys. Rev. Lett.*, vol. 13, p. 479, 1964.
- [3] J. D. Joannopoulos, R. D. Meade, , and J. N. Winn, *Photonic Crystals, Molding the Flow of Light*. NJ: Princeton University Press, 2008.
- [4] P. A. Franken and J. F. Ward, “Optical harmonics and nonlinear phenomena,” *Rev. Mod. Phys.*, vol. 35, p. 23, 1963.
- [5] E. Glavas, J. M. Cabrera, and P. D. Townsend, “A comparison of optical damage in different types of LiNbO₃ waveguides,” *J. Phys. D: Appl. Phys.*, vol. 22, p. 611, 1989.
- [6] K. Sakoda, *Optical Properties of Photonic Crystals*. Berlin: Springer, 2001.
- [7] T. F. Krauss, R. M. D. L. Rue, and S. Brand, “Two-dimensional photonic-bandgap structures operating at near-infrared wavelengths,” *Nature*, vol. 383, p. 699, 1996.
- [8] J. S. Foresi, P. R. Villeneuve, J. Ferrera, E. R. Thoen, G. Steinmeyer, S. Fan, J. D. Joannopoulos, L. C. Kimerling, H. Smith, and E. P. Ippen, “Photonic-bandgap microcavities in optical waveguides,” *Nature*, vol. 390, p. 143, 1997.
- [9] Y. Yi, P. Bermel, K. Wada, X. Duan, J. D. Joannopoulos, and L. C. Kimerling, “Tunable multichannel optical filter based on silicon photonic band gap materials actuation,” *Appl. Phys. Lett.*, vol. 81, no. 22, p. 4112, 2002.
- [10] M. H. Shih, W. J. Kim, W. Kuang, J. R. Cao, H. Yukawa, S. J. Choi, J. D. O’Brien, P. D. Dapkus, and W. K. Marshall, “Two-dimensional photonic crystal mach–zehnder interferometers,” *Appl. Phys. Lett.*, vol. 84, no. 4, p. 460, 2004.
- [11] O. Painter, R. K. Lee, A. Scherer, A. Yariv, J. D. O’Brien, P. D. Dapkus, and I. Kim, “Two-Dimensional Photonic Band-Gap Defect Mode Laser,” *Science*, vol. 284, no. 5421, p. 1819, 1999.
- [12] E. Miyai, K. Sakai, T. Okano, W. Kunishi, D. Ohnishi, , and S. Noda, “Photonicslasers producing tailored beams,” *Nature*, vol. 441, p. 946, 2006.

- [13] T. D. Happ, M. Kamp, A. Forchel, J.-L. Gentner, and L. Goldstein, "Two-dimensional photonic crystal coupled-defect laser diode," *Appl. Phys. Lett.*, vol. 82, no. 1, p. 4, 2003.
- [14] X. Hu, Q. Zhang, Y. Liu, B. Cheng, and D. Zhang, "Ultrafast three-dimensional tunable photonic crystal," *Appl. Phys. Lett.*, vol. 83, no. 13, p. 2518, 2003.
- [15] S. W. Leonard, H. M. van Driel, J. Schilling, and R. B. Wehrspohn, "Ultrafast band-edge tuning of a two-dimensional silicon photonic crystal via free-carrier injection," *Phys. Rev. B*, vol. 66, no. 16, p. 161102, 2002.
- [16] E. Graugnard, S. N. Dunham, J. S. King, D. Lorang, S. Jain, and C. J. Summers, "Enhanced tunable bragg diffraction in large-pore inverse opals using dual-frequency liquid crystal," *Appl. Phys. Lett.*, vol. 91, no. 11, p. 111101, 2007.
- [17] T. V. Murzina, F. Y. Sychev, I. A. Kolmychek, and O. A. Aktsipetrov, "Tunable ferroelectric photonic crystals based on porous silicon templates infiltrated by sodium nitrite," *Applied Physics Letters*, vol. 90, no. 16, p. 161120, 2007.
- [18] S.-L. Kuai, G. Bader, and P. V. Ashrit, "Tunable electrochromic photonic crystals," *Appl. Phys. Lett.*, vol. 86, no. 22, p. 221110, 2005.
- [19] V. Morandi, F. Marabelli, V. Amendola, M. Meneghetti, and D. Comoretto, "Colloidal photonic crystals doped with gold nanoparticles: Spectroscopy and optical switching properties," *Adv. Funct. Mater.*, vol. 17, no. 15, p. 2779, 2007.
- [20] V. Morandi, F. Marabelli, V. Amendola, M. Meneghetti, and D. Comoretto, "Light localization effect on the optical properties of opals doped with gold nanoparticles," *J. Phys. Chem. C*, vol. 112, no. 16, p. 6293, 2008.
- [21] V. Amendola, G. A. Rizzi, S. Polizzi, and M. Meneghetti, "Synthesis of gold nanoparticles by laser ablation in toluene: quenching and recovery of the surface plasmon absorption," *J. Phys. Chem. B*, vol. 109, no. 49, p. 23125, 2005.
- [22] V. Amendola and M. Meneghetti, "Controlled size manipulation of free gold nanoparticles by laser irradiation and their facile bioconjugation," *J. Mat. Chem.*, vol. 17, no. 44, p. 4705, 2007.
- [23] J. S. Hayden and N. Neuroth, in *The properties of optical glass*, eds. M. Bach and N. Neuroth. Berlin, Germany: Springer-Verlag, 1995.
- [24] M. E. Lines, "Oxide glasses for fast photonic switching: A comparative study," *J. Appl. Phys.*, vol. 69, p. 6876, 1991.
- [25] C. B. de Araujo, E. L. Falcao-Filho, A. Humeau, D. Guichaoua, G. Boudebs, and L. R. P. Kassab, "Picosecond third-order nonlinearity of lead-oxide glasses in the infrared," *Appl. Phys. Lett.*, vol. 87, p. 221904, 2005.
- [26] G. I. Stegeman and M. Segev, "Optical spatial solitons and their interactions: Universality and diversity," *Science*, vol. 286, p. 1518, 1999.

- [27] S. Trillo and W. E. Torruellas, *Spatial Solitons*. Berlin, Germany: Springer-Verlag, 2001.
- [28] C. Conti and G. Assanto, *Nonlinear Optics Applications: Bright Spatial Solitons, in Encyclopedia of Modern Optics*, eds. R. D. Guenther, D. G. Steel and L. Bayvel, vol. 5. Oxford, UK: Elsevier, 2004.
- [29] Y. S. Kivshar and G. P. Agrawal, *Optical Solitons*. San Diego, USA: Academic Press, 2003.
- [30] P. L. Kelley, "Self-focusing of optical beams," *Phys. Rev. Lett.*, vol. 15, p. 1005, 1965.
- [31] C. Conti, M. Peccianti, and G. Assanto, "Route to nonlocality and observation of accessible solitons," *Phys. Rev. Lett.*, vol. 91, p. 73901, 2003.
- [32] S. Tzortzakis, L. Sudrie, M. Franco, B. Prade, A. Mysyrowicz, A. Couairon, and L. Bergé, "Self-guided propagation of ultrashort IR laser pulses in fused silica," *Phys. Rev. Lett.*, vol. 87, p. 213902, 2001.
- [33] S. Tzortzakis, L. Bergé, A. Couairon, M. Franco, B. Prade, and A. Mysyrowicz, "Breakup and fusion of self-guided femtosecond light pulses in air," *Phys. Rev. Lett.*, vol. 86, p. 5470, 2001.
- [34] C. Rotschild, O. Cohen, O. Manela, M. Segev, and T. Carmon, "Solitons in non-linear media with an infinite range of nonlocality: First observation of coherent elliptic solitons and of vortex-ring solitons," *Phys. Rev. Lett.*, vol. 95, p. 213904, 2005.
- [35] Z. Chen, M. Asaro, O. Ostroverkhova, W. E. Moerner, M. He, and R. J. Twieg, "Self-trapping of light in a photorefractive organic glass," *Opt. Lett.*, vol. 28, p. 2509, 2003.
- [36] Y. S. Kivshar and G. I. Stegeman, "Spatial optical solitons - guiding light for future technologies," *Opt. Photon. News*, vol. 13, p. 59, 2002.
- [37] M. Peccianti, A. Dyadyusha, M. Kaczmarek, and G. Assanto, "Tunable refraction and reflection of self-confined light beams," *Nat. Phys.*, vol. 2, p. 737, 2006.
- [38] P. V. Mamyshev, A. Villeneuve, G. I. Stegeman, and J. S. Aitchison, "Steerable optical waveguides formed by bright spatial solitons in AlGaAs," *Electron. Lett.*, vol. 30, p. 726, 1994.
- [39] L. Friedrich, G. I. Stegeman, P. Millar, C. J. Hamilton, and J. S. Aitchison, "Dynamic, electronically controlled angle steering of spatial solitons in AlGaAs slab waveguides," *Opt. Lett.*, vol. 23, p. 1438, 1998.
- [40] M. Shalaby and A. Barthelemy, "Experimental spatial soliton trapping and switching," *Opt. Lett.*, vol. 16, p. 1472, 1991.

- [41] W. Krolikowski and Y. S. Kivshar, "Soliton-based optical switching in waveguide arrays," *J. Opt. Soc. Am. B*, vol. 13, p. 876, 1996.
- [42] A. Fratalocchi, G. Assanto, K. A. Brzdakiewicz, and M. A. Karpierz, "All-optical switching and beam steering in tunable waveguide arrays," *Appl. Phys. Lett.*, vol. 86, p. 051112, 2005.
- [43] K. W. D. Long, K. B. Rochford, and G. I. Stegeman, "Effect of 2-photon absorption on all-optical guided-wave devices," *Appl. Phys. Lett.*, vol. 55, p. 1823, 1989.
- [44] A. Dubietis, E. Gaizauskas, G. Tamosauskas, and P. DiTrapani, "Light filaments without self-channeling," *Phys. Rev. Lett.*, vol. 92, p. 253903, 2004.
- [45] H. S. Eisenberg, R. Morandotti, Y. Silberberg, S. Bar-Ad, D. Ross, and J. S. Aitchison, "Kerr spatiotemporal self-focusing in a planar glass waveguide," *Phys. Rev. Lett.*, vol. 87, p. 043902, 2001.
- [46] J. S. Aitchison, D. C. Hutchings, J. U. Kang, G. I. Stegeman, and A. Villeneuve, "The nonlinear optical properties of AlGaAs at the half band gap," *IEEE J. Quantum Electron.*, vol. 33, p. 341, 1997.
- [47] D. C. Hutchings, J. S. Aitchison, and J. M. Arnold, "Nonlinear refractive coupling and vector solitons in anisotropic cubic media," *J. Opt. Soc. Am. B*, vol. 14, p. 869, 1997.
- [48] A. S. Rodrigues, M. Santagiustina, and E. M. Wright, "Femtosecond pulse propagation and optical solitons in semiconductor-doped glass waveguides in the vicinity of a two-photon resonance," *Opt. Quantum Electron.*, vol. 29, p. 961, 1997.
- [49] A. N. Belanger, A. Villeneuve, and J. S. Aitchison, "Solitonlike pulses in self-defocusing AlGaAs waveguides," *J. Opt. Soc. Am. B*, vol. 14, p. 3003, 1997.
- [50] V. I. Bespalov and V. I. Talanov, "Filamentary structure of light beams in nonlinear liquids," *JETP Lett.*, vol. 3, p. 307, 1966.
- [51] M. Peccianti, C. Conti, and G. Assanto, "Optical multisoliton generation in nematic liquid crystals," *Opt. Lett.*, vol. 28, p. 2231, 2003.
- [52] M. Peccianti, C. Conti, G. Assanto, A. D. Luca, and C. Umeton, "Routing of highly anisotropic spatial solitons and modulational instability in liquid crystals," *Nature*, vol. 432, p. 733, 2004.
- [53] W. Press, S. Teukolsky, W. Vetterling, and B. Flannery, *Numerical Recipes in C*. Cambridge, UK: Cambridge University Press, 2nd ed., 1992.
- [54] J. Gonzalo, O. Sanz, A. Perea, J. M. Fernandez-Navarro, C. N. Afonso, and J. Garcia-Lopez, "High refractive index and transparent heavy metal oxide glassy thin films," *Appl. Phys. A*, vol. 76, p. 943, 2003.

- [55] E. Yablonovitch and N. Bloembergen, "Avalanche ionization and the limiting diameter of filaments induced by light pulses in transparent media," *Phys. Rev. Lett.*, vol. 29, p. 907, 1972.
- [56] N. Bloembergen, "Laser-induced breakdown in solids," *IEEE J. Quantum Electron.*, vol. 10, p. 375, 1974.
- [57] J. Siegel, J. M. Fernandez-Navarro, A. Garcia-Navarro, V. Diez-Blanco, O. Sanz, J. Solis, F. Vega, and J. Armengol, "Waveguide structures in heavy metal oxide glass written with femtosecond laser pulses above the critical self-focusing threshold," *Appl. Phys. Lett.*, vol. 86, p. 121109, 2005.
- [58] G. Fibich and A. L. Gaeta, "Critical power for self-focusing in bulk media and hollow waveguides," *Opt. Lett.*, vol. 25, p. 335, 2000.
- [59] B. C. Stuart, M. D. Feit, A. M. Rubenchik, B. W. Shore, and M. D. Perry, "Laser-induced damage in dielectrics with nanosecond to subpicosecond pulses," *Phys. Rev. Lett.*, vol. 74, p. 2248, 1995.
- [60] B. C. Stuart, M. D. Feit, S. Herman, A. M. Rubenchik, B. W. Shore, and M. D. Perry, "Nanosecond-to-femtosecond laser-induced breakdown in dielectrics," *Phys. Rev. B*, vol. 53, p. 1749, 1996.
- [61] X. Liu, D. B. Hollis, and J. McDougall, "Ultraviolet absorption edge studies of heavy metal oxide glasses," *Phys. Chem. Glasses*, vol. 37, p. 160, 1996.
- [62] K. Saito and A. J. Ikushima, "Absorption edge in silica glass," *Phys. Rev. B*, vol. 62, p. 8584, 2000.
- [63] R. DeSalvo, A. A. Said, D. J. Hagan, E. W. VanStryland, and M. Sheik-Bahae, "Infrared to ultraviolet measurements of two-absorption and n_2 in wide bandgap solids," *IEEE J. Quantum. Electron.*, vol. 32, p. 1324, 1996.
- [64] M. A. Porras, A. Parola, D. Faccio, A. Dubietis, and P. DiTrapani, "Nonlinear unbalanced Bessel beams: Stationary conical waves supported by nonlinear losses," *Phys. Rev. Lett.*, vol. 93, p. 153902, 2004.
- [65] M. Centurion, Y. Pu, M. Tsang, and D. Psaltis, "Dynamics of filament formation in a Kerr medium," *Phys. Rev. A*, vol. 71, p. 063811, 2005.
- [66] S. Skupin, L. Bergé, U. Peschel, F. Lederer, G. Mejean, J. Yu, J. Kasparian, E. Salmon, J. P. Wolf, M. Rodriguez, L. Woeste, R. Bourayou, and R. Sauerbrey, "Filamentation of femtosecond light pulses in the air: Turbulent cells versus long-range clusters," *Phys. Rev. E*, vol. 70, p. 046602, 2004.
- [67] M. Centurion, Y. Pu, and D. Psaltis, "Self-organization of spatial solitons," *Opt. Express*, vol. 13, p. 6202, 2005.
- [68] L. Guyon, F. Courvoisier, V. Boutou, R. Nuter, A. Vinçotte, S. Champeaux, L. Bergé, P. Glorieux, and J. P. Wolf, "Self-organized bundle of lasing filaments

- in dense media,” *Phys. Rev. A*, vol. 73, p. 051802, 2006.
- [69] A. Dubietis, E. Kucinskas, G. Tamosauskas, E. Gaizauskas, M. A. Porras, and P. DiTrapani, “Self-reconstruction of light filaments,” *Opt. Lett.*, vol. 29, p. 2893, 2004.
- [70] G. Stegeman and G. Assanto, “Nonlinear integrated optical devices,” in *and Components: Design and Application* (E. J. Murphy, ed.), pp. 381–418, Dekker, 1999.
- [71] E. Lim, M. Fejer, and R. Byer, “Second-harmonic generation of green light in periodically poled planar lithium niobate waveguide,” *Electron. Lett.*, vol. 25, no. 3, pp. 174–175, 1989.
- [72] M. Yamada, N. Nada, M. Saitoh, and K. Watanabe, “First-order quasi-phase matched LiNbO₃ waveguide periodically poled by applying an external field for efficient blue second-harmonic generation,” *Appl. Phys. Lett.*, vol. 62, p. 435, 1993.
- [73] S. Miyazawa, “Ferroelectric domain inversion in Ti-diffused LiNbO₃ optical waveguide,” *J. Appl. Phys.*, vol. 50, p. 4599, 1979.
- [74] A. C. Busacca, C. L. Sones, R. W. Eason, and S. Mailis, “First-order quasi-phase-matched blue light generation in surface-poled Ti:indiffused lithium niobate waveguides,” *Appl. Phys. Lett.*, vol. 84, p. 4430, 2004.
- [75] Y. J. Ding, S. J. Lee, and J. B. Khurgin, “Transversely pumped counterpropagating optical parametric oscillation and amplification,” *Phys. Rev. Lett.*, vol. 75, p. 429, 1995.
- [76] C. Conti, G. Assanto, and S. Trillo, “Cavityless oscillation through backward quasi-phase-matched second-harmonic generation,” *Opt. Lett.*, vol. 24, p. 1139, 1999.
- [77] K. Gallo, P. Baldi, M. D. Micheli, D. B. Ostrowsky, and G. Assanto, “Cascading phase shift and multivalued response in counterpropagating frequency-nondegenerate parametric amplifiers,” *Opt. Lett.*, vol. 25, p. 966, 2000.
- [78] G. D. Landry and T. A. Maldonado, “Counterpropagating quasi-phase matching: a generalized analysis,” *J. Opt. Soc. Am. B*, vol. 21, p. 1509, 2004.
- [79] A. C. Busacca, C. L. Sones, V. Apostolopoulos, R. W. Eason, and S. Mailis, “Surface domain engineering in congruent lithium niobate single crystals: A route to submicron periodic poling,” *Appl. Phys. Lett.*, vol. 81, p. 4946, 2002.
- [80] A. C. Busacca, A. C. Cino, S. Riva-Sanseverino, M. Ravaro, and G. Assanto, “Silica masks for improved surface poling of lithium niobate,” *Electron. Lett.*, vol. 41, p. 92, 2005.
- [81] A. Yariv, *Optical Electronics in Modern Communications*. New York, USA: Oxford University Press, 1997.

- [82] M. M. Fejer, G. A. Magel, D. H. Jundt, and R. L. Byer, "Quasi-phase-matched second harmonic generation: tuning and tolerances," *IEEE J. Quantum Electron.*, vol. 28, p. 2631, 1992.
- [83] M. D. Micheli, D. B. Ostrowsky, J. P. Baretty, C. Canali, A. Carnera, G. Mazzi, and M. Papuchon, "Crystalline and optical quality of protonexchanged waveguides," *J. Lightwave Technol.*, vol. LT-4, p. 743, 1986.
- [84] L. Chanvillard, P. Aschiéri, P. Baldi, D. B. Ostrowsky, M. de Micheli, L. Huang, and D. J. Bamford, "Soft proton exchange on periodically poled LiNbO₃: A simple waveguide fabrication process for highly efficient nonlinear interactions," *Appl. Phys. Lett.*, vol. 76, p. 1089, 2000.
- [85] R. DeSalvo, D. J. Hagan, M. Sheik-Bahae, G. I. Stegeman, E. W. V. Stryland, and H. Vanherzeele, "Self-focusing and self-defocusing by cascaded second-order effects in KTP," *Opt. Lett.*, vol. 17, p. 28, 1992.
- [86] G. I. Stegeman, M. Sheik-Bahae, E. V. Stryland, and G. Assanto, "Large nonlinear phase shifts in second-order nonlinear-optical processes," *Opt. Lett.*, vol. 18, p. 13, 1993.
- [87] G. Assanto, G. I. Stegeman, M. Sheik-Bahae, and E. VanStryland, "Coherent interactions for all-optical signal processing via quadratic nonlinearities," *IEEE J. Quantum Electron.*, vol. 31, p. 673, 1995.
- [88] G. Assanto and G. Stegeman, "Nonlinear optics basics: cascading," in *Encyclopedia of Modern Optics* (R. D. Guenther, D. G. Steel, and L. D. Bayvel, eds.), vol. 3, pp. 207–212, Elsevier, 2005.
- [89] R. W. Boyd, *Nonlinear Optics, second edition*. San Diego, USA: Academic Press, 2003.
- [90] T. Suhara and H. Nishihara, "Theoretical analysis of waveguide second-harmonic generation phase matched with uniform and chirped gratings," *IEEE J. Quantum Electron.*, vol. 26, p. 1265, 1990.
- [91] X. F. Cao, R. V. Ramaswamy, and R. Srivastava, "Characterization of annealed proton exchanged LiNbO₃ waveguides for nonlinear frequency conversion," *J. Lightwave Technol.*, vol. 10, p. 1302, 1992.
- [92] Y. N. Korkishko, V. A. Fedorov, M. P. D. Micheli, P. Baldi, K. E. Hadi, and A. Leycuras, "Relationships between structural and optical properties of proton-exchanged waveguides on z-cut lithium niobate," *Appl. Opt.*, vol. 35, p. 7056, 1996.
- [93] I. Shoji, T. Kondo, A. Kitamoto, M. Shirane, and R. Ito, "Absolute scale of second-order nonlinear-optical coefficients," *J. Opt. Soc. Am. B*, vol. 14, p. 2268, 1997.

- [94] J. T. Manassah and O. R. Cockings, "Induced phase modulation of a generated second-harmonic signal," *Opt. Lett.*, vol. 12, p. 1005, 1987.
- [95] S. Cussat-Blanc, R. M. Rassoul, A. Ivanov, E. Freysz, and A. Ducasse, "Influence of cascading phenomena on a type I second-harmonic wave generated by an intense femtosecond pulse: application to the measurement of the effective second-order coefficient," *Opt. Lett.*, vol. 23, p. 1585, 1998.
- [96] A. Kobayakov, U. Peschel, R. Muschall, G. Assanto, V. P. Torchigin, and F. Lederer, "Analytical approach to all-optical modulation by cascading," *Opt. Lett.*, vol. 20, p. 1686, 1995.
- [97] G. Assanto, Z. Wang, D. J. Hagan, and E. W. VanStryland, "All-optical modulation via nonlinear cascading in type II second-harmonic generation," *Appl. Phys. Lett.*, vol. 67, p. 2120, 1995.
- [98] G. Assanto, "Transistor action through nonlinear cascading in type II interactions," *Opt. Lett.*, vol. 20, no. 15, p. 1595, 1995.
- [99] J. Meyn, C. Laue, R. Knappe, R. Wallenstein, and M. Fejer, "Fabrication of periodically poled lithium tantalate for uv generation with diode lasers," *Appl. Phys. B*, vol. 73, no. 2, p. 111, 2001.
- [100] A. V. Buryak, P. D. Trapani, D. V. Skryabin, and S. Trillo, "Optical solitons due to quadratic nonlinearities: from basic physics to futuristic applications," *Phys. Rep.*, vol. 370, p. 63, 2002.
- [101] W. E. Torruellas, Z. Wang, D. J. Hagan, E. M. VanStryland, G. I. Stegeman, L. Torner, and C. R. Menyuk, "Observation of two-dimensional spatial solitary waves in a quadratic medium," *Phys. Rev. Lett.*, vol. 74, p. 5036, 1995.
- [102] R. Schiek, Y. Baek, and G. I. Stegeman, "One-dimensional spatial solitary waves due to cascaded second-order nonlinearities in planar waveguides," *Phys. Rev. E*, vol. 53, p. 1138, 1996.
- [103] P. Olver, *Applications of Lie groups to differential equations*. New York, USA: Springer-Verlag, 1986.
- [104] G. Bluman, *Symmetries and Differential Equations*. Springer. New York, USA: Springer-Verlag, 1989.
- [105] E. A. Kuznetsov, A. M. Rubenchik, and V. E. Zakharov, "Soliton stability in plasmas and hydrodynamics," *Physics Reports*, vol. 142, no. 3, pp. 103 – 165, 1986.
- [106] D. E. Pelinovsky, A. V. Buryak, and Y. S. Kivshar, "Instability of solitons governed by quadratic nonlinearities," *Phys. Rev. Lett.*, vol. 75, pp. 591–595, Jul 1995.
- [107] F. Baronio, C. D. Angelis, P.-H. Pioger, V. Couderc, and A. Barthélémy, "Reflection of quadratic solitons at the boundary of nonlinear media," *Opt. Lett.*, vol. 29,

- no. 9, pp. 986–988, 2004.
- [108] A. D. Capobianco, C. D. Angelis, A. L. Palma, and G. F. Nalesso, “Beam dynamics at the interface between second-order nonlinear dielectrics,” *J. Opt. Soc. Am. B*, vol. 14, no. 8, pp. 1956–1960, 1997.
 - [109] Y. V. Kartashov, V. A. Vysloukh, and L. Torner, “Soliton modes, stability, and drift in optical lattices with spatially modulated nonlinearity,” *Opt. Lett.*, vol. 33, no. 15, pp. 1747–1749, 2008.
 - [110] F. K. Abdullaev and J. Garnier, “Propagation of matter-wave solitons in periodic and random nonlinear potentials,” *Phys. Rev. A*, vol. 72, no. 6, p. 061605, 2005.
 - [111] H. Sakaguchi and B. A. Malomed, “Matter-wave solitons in nonlinear optical lattices,” *Phys. Rev. E*, vol. 72, no. 4, p. 046610, 2005.
 - [112] G. Fibich, Y. Sivan, and M. Weinstein, “Bound states of nonlinear schrödinger equations with a periodic nonlinear microstructure,” *Physica D: Nonlinear Phenomena*, vol. 217, no. 1, pp. 31 – 57, 2006.
 - [113] N. G. Vakhitov and A. A. Kolokolov, “Stationary solutions of the wave equation in a medium with nonlinearity saturation,” *Radiophys. and Quantum Electron.*, vol. 16, p. 783, 1973.
 - [114] A. A. Kanashov and A. M. Rubenchik, “On diffraction and dispersion effect on three wave interaction,” *Physica D: Nonlinear Phenomena*, vol. 4, no. 1, pp. 122 – 134, 1981.
 - [115] C. Etrich, U. Peschel, F. Lederer, and B. A. Malomed, “Stability of temporal chirped solitary waves in quadratically nonlinear media,” *Phys. Rev. E*, vol. 55, pp. 6155–6161, May 1997.
 - [116] A. V. Buryak, Y. S. Kivshar, and S. Trillo, “Stability of three-wave parametric solitons in diffractive quadratic media,” *Phys. Rev. Lett.*, vol. 77, p. 5210, 1996.
 - [117] D. Mihalache, D. Mazilu, L.-C. Crasovan, and L. Torner, “Walking solitons in type ii second-harmonic generation,” *Phys. Rev. E*, vol. 56, pp. R6294–R6297, Dec 1997.
 - [118] L. Landau and E. M. Lifshitz, *Quantum Mechanics (Non-Relativistic Theory)*. New York, USA: Pergamon Press, 1965.
 - [119] L. Torner, D. Mazilu, and D. Mihalache, “Walking solitons in quadratic nonlinear media,” *Phys. Rev. Lett.*, vol. 77, p. 2455, 1996.
 - [120] C. Conti, S. Trillo, P. D. Trapani, J. Kilius, A. Bramati, S. Minardi, W. Chinaglia, and G. Valiulis, “Effective lensing effects in parametric frequency conversion,” *J. Opt. Soc. Am. B*, vol. 19, no. 4, pp. 852–859, 2002.

- [121] P. D. Trapani, A. Bramati, S. Minardi, W. Chinaglia, C. Conti, S. Trillo, J. Kilius, and G. Valiulis, "Focusing versus defocusing nonlinearities due to parametric wave mixing," *Phys. Rev. Lett.*, vol. 87, p. 183902, 2001.
- [122] C. B. Clausen, O. Bang, and Y. S. Kivshar, "Spatial solitons and induced Kerr effects in quasi-phase-matched quadratic media," *Phys. Rev. Lett.*, vol. 78, p. 4749, 1997.
- [123] K. Gallo, C. Codemard, C. B. Gawith, J. Nilsson, P. G. R. Smith, N. G. R. Broderick, and D. J. Richardson, "Guided-wave second-harmonic generation in a LiNbO_3 nonlinear photonic crystal," *Opt. Lett.*, vol. 31, p. 1232, 2006.